
PHYSICS-AWARE NEURAL IMPLICIT SOLVERS FOR MULTISCALE, PARAMETRIC PDEs WITH APPLICATIONS IN HETEROGENEOUS MEDIA. *

Matthaios Chatzopoulos^a, Phaedon-Stelios Koutsourelakis^{a,b,*}

^a Technical University of Munich, Professorship of Data-driven Materials Modeling,
School of Engineering and Design, Boltzmannstr. 15, 85748 Garching, Germany

^b Munich Data Science Institute (MDSI - Core member), Garching, Germany

ABSTRACT

We propose Physics-Aware Neural Implicit Solvers (PANIS), a novel, data-driven framework for learning surrogates for parametrized Partial Differential Equations (PDEs). It consists of a probabilistic, learning objective in which weighted residuals are used to probe the PDE and provide a source of *virtual* data i.e. the actual PDE never needs to be solved. This is combined with a physics-aware implicit solver that consists of a much coarser, discretized version of the original PDE, which provides the requisite information bottleneck for high-dimensional problems and enables generalization in out-of-distribution settings (e.g. different boundary conditions). We demonstrate its capability in the context of random heterogeneous materials where the input parameters represent the material microstructure. We extend the framework to multiscale problems and show that a surrogate can be learned for the effective (homogenized) solution without ever solving the reference problem. We further demonstrate how the proposed framework can accommodate and generalize several existing learning objectives and architectures while yielding probabilistic surrogates that can quantify predictive uncertainty.

Keywords Random Heterogeneous Materials · Data-driven · Probabilistic surrogate · Deep Learning · Machine Learning · High-Dimensional Surrogates · Virtual Observables.

1 Introduction

Parametric PDEs appear in a wide variety of problems of engineering relevance, and their repeated solution under different parametric values in the context of many-query applications represents a major computational roadblock in achieving analysis and design objectives. Perhaps one of the most challenging applications, which lies at the core of this investigation, is encountered in the context of (random) heterogeneous media in which microstructural details determine their macroscopic properties [1]. These are found in a multitude of engineering applications, such as aligned and chopped fiber composites, porous membranes, particulate composites, cellular solids, colloids, microemulsions, concrete [1]. Their microstructural properties can vary, most often randomly, at multiple length-scales [2]. Capturing this variability requires, in general, very high-dimensional representations and very fine discretizations, which in turn imply a significant cost for each solution of the governing PDEs in order to predict their response [3]. Being able to efficiently obtain accurate solutions under varying microstructures represents a core challenge that can enable the solution of various forward analysis problems such as uncertainty quantification [4, 5]. More importantly, however, it is of relevance in the context of inverse design where one attempts to identify (families of) microstructures that achieve extremal or target properties [6]. While several different tools come into play, *data-driven* strategies, to which our contribution belongs, have risen into prominence in recent years [7, 8] as in many cases they have produced high-throughput, forward-model surrogates which are essential for inverting the microstructure-to-property link [9].

*Corresponding author

Email addresses: matthaios.chatzopoulos@tum.de (Matthaios Chatzopoulos),
p.s.koutsourelakis@tum.de (Phaedon-Stelios Koutsourelakis)

One way to categorize pertinent methods is based on the learning objectives employed which range between purely data-based to physics-informed. In the first category belong methods that rely on *labeled* data, i.e. input-output pairs [10, 11, 12, 13, 14] and cast the problem as a supervised learning task. Associated models and tools have reached a high-level of maturity and sophistication in the machine learning community and exhibit a comparatively faster and more stable training [15]. If the models employed, which usually take the form of a Deep Neural Network (DNN), are agnostic of the physical problem, their predictive accuracy is generally dependent on the amount of training data. However, unlike typical machine learning applications, as e.g. in language or vision, where data is abundant and inexpensive, in parametric PDEs, data acquisition is de facto expensive, and the reduction of the requisite number of PDE-solves one of the primary objectives [16].

On the other side of the spectrum lie physics-informed learning protocols [17, 18, 19]. These employ the PDE itself, usually in the form of collocation-type residuals, in the training loss, although energy functionals have also been utilized [20, 21]. As such, they do not require any PDE-solves and exhibit better generalization performance, but empirical results have shown that the use of labeled data can improve their performance [20]. In the works of [17], [22], [23], [21], [24], [25] the loss function used for training the model consisted of both labeled data and residuals of the governing PDE. A detailed taxonomy [26] and review regarding the application of deep, physics-informed models for solving pertinent problems can be found in [15]. The relative weights of the residual-based, data-driven and regularization terms in the loss are generally ad hoc and fine-tuned through trial and error. Furthermore, no quantification of the informational content of the residuals employed is directly available, and in general, a large number of collocation points is needed.

Another aspect of the problem that plays a pivotal role is the dimension of the parametric input. In cases where this is low to medium, generic, traditional architectures such as Gaussian Processes [27], exhibit good results. Dimensionality reduction offers an avenue for overcoming difficulties in high-dimensional problems and several such strategies have been developed [28, 29, 30, 31]. Since, in general, dimensionality reduction is performed in a separate step, if the lower-dimensional features identified are not affecting the response/properties, their utility is limited [32]. Furthermore, most of the attention has been directed towards reducing the dimensionality of the entities involved [33] rather than reducing, or better yet, coarse-graining, the physical models [34].

Recent advances in deep learning [35] have triggered a big effort towards the utilization of Deep Neural Networks for solving efficiently such problems [36, 37, 38]. Combining DNNs with dimensionality reduction techniques has also been employed in problems involving heterogeneous media as in [39, 40, 41]. When the input is infinite-dimensional (i.e. a function), one of the latest and most promising advancements are the so-called Neural Operators [42], which attempt to approximate directly the map to the PDE-solution, i.e. a function to function mapping between Banach spaces. Typical examples include the Deep Operator Network (DeepONet) [11] (and its physics-informed version in [18]), the Graph Neural Operator (GNO) [12], the Fourier Neural Operator (FNO) [13, 43], the Wavelet Neural Operator

[44] and the Convolutional Neural Operator [45]. While such methods promise resolution-independent results, they sample the input function on a given grid and employ a DNN to parametrize the PDE solution. As shown in [46] this can lead to systematic bias and aliasing errors which could be overcome by using truncated (i.e. finite-dimensional) Chebyshev or Fourier series for both domain and co-domain.

We note finally that most deep-learning-centered strategies have been based on transferring or improving NN architectures that parametrize the input-output map. Fewer efforts have attempted to incorporate physical inductive biases [47] in those architectures by e.g. endowing them with invariance/equivariance properties when those are available [48].

Despite notable progress, very few models are capable of producing probabilistic predictive estimates [49, 21, 50, 51]. This can be achieved by learning/approximating the posterior (given labeled data) of the model parameters, which is a difficult task given the millions or even billions of parameters that DNNs possess. Much fewer efforts attempt to learn directly a predictive posterior of the solution [21]. We believe, nevertheless, that this is very important for any data-driven scheme (even more so for over-parametrized models) given that a finite number of data points can be employed and, in fact, reducing the requisite information extracted in the form of input-output pairs or otherwise from the PDE, is one of the main objectives. Information loss that can give rise to predictive uncertainty also arises due to the processes of dimensionality reduction or model compression/reduction, which should be quantified and propagated in the estimates.

In this work, we revisit the way information from the governing PDE is ingested as well as the architecture employed to capture the sought input-output map [20]. In section 2, we propose Physics-Aware Neural Implicit Solvers (PANIS), a novel, data-driven framework which consists of a probabilistic, learning objective in which weighted residuals (section 2.1) are used to probe the PDE and provide a source of *virtual* data [23], i.e. the actual PDE never needs to be solved (section 2.2). The formulation enables us to recast the problem as one of probabilistic inference (section 2.3). We show

that selecting at random a few of those residuals at each iteration is sufficient to learn a probabilistic surrogate. While, as we discuss, various existing DNN-based architectures can be readily integrated into this framework, we advocate instead a physics-aware implicit solver (section 2.4) that consists of a (much) coarser, discretized version of the original PDE, which provides the requisite information bottleneck for high-dimensional problems and enables generalization in out-of-distribution settings (e.g. different boundary conditions). We extend the framework to multiscale problems by proposing mPANIS (section 3) and show that a surrogate can be learned for the effective (homogenized) solution without ever solving the reference problem [52]. We further demonstrate how the proposed framework can accommodate and generalize several existing learning objectives and architectures while yielding probabilistic surrogates that can quantify predictive uncertainty (sections 2.5 3.3). We substantiate its capability in the context of random heterogeneous materials where the input parameters represent the material microstructure (section 4). Apart from comparative estimates with Physics Informed Fourier Neural Operators (PINO) [43] and assessing performance with respect to the dimension of the parametric input vector, we pay special attention to problems that involve predictions under *extrapolative settings* i.e. different microstructures or boundary conditions as compared to the ones used in training. In such problems, and despite being extremely lightweight (e.g. it has up to three-orders of magnitude fewer training parameters as compared to PINO), we show that (m)PANIS can produce very accurate predictive estimates.

2 Methodology

We are concerned with parametric PDEs which can be generally written as:

$$\begin{aligned}\mathcal{L}(c(\mathbf{s}; \mathbf{x}), u(\mathbf{s})) &= 0, & \mathbf{s} \in \Omega & \quad ((\text{non})\text{linear differential operator}) \\ \mathcal{B}(c(\mathbf{s}; \mathbf{x}), u(\mathbf{s})) &= 0, & \mathbf{s} \in \partial\Omega & \quad (\text{boundary-conditions operator})\end{aligned}\tag{1}$$

where \mathbf{s} denotes space, $\Omega \subset \mathbb{R}^{d_s}$ the problem domain, $c(\mathbf{s}; \mathbf{x})$ denotes an input function parametrized by $\mathbf{x} \in \mathcal{X} \subset \mathbb{R}^{d_x}$ (e.g. microstructure or material property field) and $u(\mathbf{s})^2$ the sought solution to the boundary value problem above.

In the following, we adopt a discretized representation of the solution, i.e. $u(\mathbf{s}) \xrightarrow{\text{discretize}} \mathbf{y}$ where $\mathbf{y} \in \mathcal{Y} \subset \mathbb{R}^{d_y}$. We assume that the adopted discretization is fine enough to provide an acceptable approximation to the actual solution, which, in general, implies that $\dim(\mathbf{y}) \gg 1$. The vector \mathbf{y} could represent coefficients with respect to a given set of functions $\{\eta_i(\mathbf{s})\}_i^{d_y}$ (e.g. FE shape functions, Radial Basis Functions, Fourier, Wavelet):

$$u_{\mathbf{y}}(\mathbf{s}) = \sum_{i=1}^{d_y} y_i \eta_i(\mathbf{s}), \quad i = 1, 2, 3, \dots, d_y\tag{2}$$

or the weight/biases of a neural network. While emphasis has been directed recently on neural operators that approximate maps between infinite-dimensional, Banach spaces, we note that as demonstrated in [46], spectral neural operators can be developed by employing truncated (i.e. finite-dimensional) Chebyshev or Fourier series (i.e. when $\eta_i(\mathbf{s})$ in Equation (2) take the form of Chebyshev polynomials or sine/cosines) which can be superior in overcoming systematic bias caused by aliasing errors.

We propose Physics-Aware Neural Implicit Solvers (PANIS), a framework that casts the problem of developing surrogates for parametrized PDEs as one of probabilistic inference and which relies on the use of:

- weighted residuals as virtual data (i.e. we never use *labeled* data in the form of solution pairs (\mathbf{x}, \mathbf{y})) which are ingested probabilistically with the help of a virtual likelihood, and
- an implicit solver at the core of the probabilistic surrogate constructed which provides the requisite information bottleneck in order to deal with high-dimensional problems (i.e. when $d_x, d_y \gg 1$) and to generalize in out-of-distribution settings.

The output of PANIS is a *probabilistic* surrogate, which will be expressed in the form of a density $q(\mathbf{y}|\mathbf{x})$ that can predict the (discretized) solution for any input \mathbf{x} . We note that the predictive uncertainty in this case is not due to aleatoric stochasticity in the governing equations (although such cases can be accommodated as well) but of epistemic nature due to the use of partial, and generally small, data in constructing this surrogate as explained in the sequel.

2.1 Strong and Weak form of a boundary-value problem

We view the governing PDE as an infinite source of information, which we probe with the help of *weighted residuals*. These constitute the (virtual) data with which we attempt to train our surrogate. In order to illustrate this concretely and

²The solution $u(\mathbf{s})$ implicitly depends on the parametric input \mathbf{x} which we omit in order to simplify the notation.

clearly, we use as an example a linear, elliptic PDE. The methodological elements can then be generalized to other types of PDEs. In particular, we consider the boundary value problem:

$$\begin{aligned} \nabla(-c(\mathbf{s}; \mathbf{x}) \nabla u(\mathbf{s})) &= g, & \mathbf{s} \in \Omega \\ u(\mathbf{s}) &= u_0, & \mathbf{s} \in \Gamma_u \\ -c(\mathbf{s}; \mathbf{x}) \nabla u(\mathbf{s}) \mathbf{n} &= q_0, & \mathbf{s} \in \Gamma_q = \partial\Omega - \Gamma_u \end{aligned} \quad (3)$$

where $c(\mathbf{s}; \mathbf{x})$ is a (random) conductivity/permeability/diffusivity field which depends on the parameters \mathbf{x} . We denote with Γ_u and Γ_q the parts of the boundary where Dirichlet and Neumann conditions are respectively defined. The symbol \mathbf{n} indicates the outward, unit normal vector while the u_0 and q_0 denote the prescribed values.

We employ candidate solutions $u_{\mathbf{y}}$ which are represented by the finite-dimensional $\mathbf{y} \in \mathbb{R}^{d_y}$ as discussed above and which are assumed to a priori satisfy the Dirichlet BCs³. These are combined with weighting functions $w(\mathbf{s}) \in \mathcal{W}$ which are assumed to be zero at the Dirichlet boundary i.e. $w(\mathbf{s})|_{\mathbf{s} \in \Gamma_u} = 0$.

By employing integration-by-parts [53] and for each such $w(\mathbf{s})$ we obtain the weighted residual:

$$r_w(\mathbf{y}, \mathbf{x}) = 0 = \int_{\Gamma_q} w q_0 d\Gamma + \int_{\Omega} \nabla w c(\mathbf{s}; \mathbf{x}) \nabla u_{\mathbf{y}} d\mathbf{s} - \int_{\Omega} w g d\mathbf{s}. \quad (4)$$

We note that depending on the choice of the weight functions w (at least) six methods (i.e. collocation, sub-domain, least-squares, (Petrov)-Galerkin, moments) arise as special cases [53]. As it will become apparent in the sequel, the weighted residuals are used as data sources and not in the traditional sense, i.e. to derive a discretized system of equations for the approximate solution of the problem. Hence, we would be at liberty to consider alternate or even non-symmetric versions with respect to $u_{\mathbf{y}}$ and w as for example expressions with lower-order derivatives of the candidate solution $u_{\mathbf{y}}$, which are obtained by applying further integration-by-parts [54].

2.2 Virtual Observables and Virtual Likelihood

Rather than solving the governing equations multiple times for different values of \mathbf{x} in order to obtain a *labeled* training dataset (i.e. pairs of (\mathbf{x}, \mathbf{y})) we treat weighted residuals as in Equation (4) as *virtual observables* [23]. In particular, given N distinct weighting function w_j and the corresponding residuals $r_{w_j}(\mathbf{y}, \mathbf{x})$, we assume that their values \hat{r}_j have been *virtually* observed and are equal to 0. The *virtual* observables $\hat{\mathbf{R}} = \{\hat{r}_j = 0\}_{j=1}^N$ imply a *virtual* likelihood which is assumed to be of the form:

$$\begin{aligned} p(\hat{\mathbf{R}}|\mathbf{y}, \mathbf{x}) &= \prod_{j=1}^N p(\hat{r}_j = 0|\mathbf{y}, \mathbf{x}) \\ &= \prod_{j=1}^N \frac{\lambda}{2} e^{-\lambda|r_{w_j}(\mathbf{y}, \mathbf{x})|}. \end{aligned} \quad (5)$$

The role of the hyper-parameter λ is significant as it controls how the likelihood of a pair (\mathbf{x}, \mathbf{y}) will decay if the corresponding residuals $r_{w_j}(\mathbf{y}, \mathbf{x})$ are different from zero. A reasonable guideline is to set λ^{-1} equal to the tolerance value selected in a deterministic iterative solver. We note that alternative forms of the virtual likelihood are also possible (e.g. Gaussian), but the form above was found to yield better results in the numerical experiments performed. The role of the virtual observables/likelihood is to provide information from the governing equations *without* having to solve them. We discuss in the sequel how this virtual likelihood can be used to learn a surrogate and how this can be carried out by evaluating a few residuals at a time (i.e. without ever solving the weak form).

2.3 Learning surrogates as probabilistic inference

Let $p(\mathbf{x})$ be a density on the parametric input. In the case of a random input, this is directly furnished by the problem definition. For deterministic problems, this could simply be a uniform density over the domain of possible values of \mathbf{x} . We complement this with a *prior* density $p(\mathbf{y}|\mathbf{x})$. In the ensuing numerical experiments, a vague, uninformative such prior was selected. We note that its role is not to provide a good approximation of the sought output \mathbf{y} given an input \mathbf{x} as this is to be achieved by the *posterior* discussed later.

The combination of the aforementioned prior densities with the virtual likelihood of Equation (5) in the context of Bayes' rule leads to the *joint* posterior $p(\mathbf{x}, \mathbf{y}|\hat{\mathbf{R}})$ as follows:

³This requirement is consistent with traditional derivations but can be readily relaxed or removed in our formulation.

$$p(\mathbf{x}, \mathbf{y} | \hat{\mathbf{R}}) = \frac{p(\hat{\mathbf{R}} | \mathbf{x}, \mathbf{y}) p(\mathbf{y} | \mathbf{x}) p(\mathbf{x})}{p(\hat{\mathbf{R}})}. \quad (6)$$

We emphasize that the posterior above is defined on the *joint* space of inputs \mathbf{x} and outputs \mathbf{y} . Apart from the effect of the prior, it assigns the highest probability to pairs of \mathbf{x} and \mathbf{y} that achieve 0 residuals as is the case when they are a solution pair of the boundary value problem.

Since the posterior is generally intractable, we advocate a Variational-Inference scheme [55], i.e. we seek an approximation from a parameterized family of densities $q_\psi(\mathbf{x}, \mathbf{y})$ by minimizing the Kullback-Leibler divergence with the exact posterior above. If ψ denotes the tunable parameters, this is equivalent to maximizing the Evidence Lower BOund (ELBO) $\mathcal{F}(\psi)$ to the log-evidence $\log p(\hat{\mathbf{R}})$ [56], i.e.:

$$\begin{aligned} \log p(\hat{\mathbf{R}}) &= \log \int p(\hat{\mathbf{R}} | \mathbf{x}, \mathbf{y}) p(\mathbf{y} | \mathbf{x}) p(\mathbf{x}) d\mathbf{y} d\mathbf{x} \\ &\geq \left\langle \log \frac{p(\hat{\mathbf{R}} | \mathbf{x}, \mathbf{y}) p(\mathbf{y} | \mathbf{x}) p(\mathbf{x})}{q_\psi(\mathbf{x}, \mathbf{y})} \right\rangle_{q_\psi(\mathbf{x}, \mathbf{y})} \\ &= \mathcal{F}(\psi), \end{aligned} \quad (7)$$

where the brackets $\langle \cdot \rangle_q$ indicate an expectation with respect to q . Substitution of Equation (5) in the expression above leads to:

$$\begin{aligned} \mathcal{F}(\psi) &= N \log \frac{\lambda}{2} - \lambda \sum_{j=1}^N \langle |r_{w_j}(\mathbf{y}, \mathbf{x})| \rangle_{q_\psi(\mathbf{x}, \mathbf{y})} + \left\langle \log \frac{p(\mathbf{y} | \mathbf{x}) p(\mathbf{x})}{q_\psi(\mathbf{x}, \mathbf{y})} \right\rangle_{q_\psi(\mathbf{x}, \mathbf{y})} \\ &= N \log \frac{\lambda}{2} - \lambda \sum_{j=1}^N \langle |r_{w_j}(\mathbf{y}, \mathbf{x})| \rangle_{q_\psi(\mathbf{x}, \mathbf{y})} - KL(q_\psi(\mathbf{x}, \mathbf{y}) || p(\mathbf{y} | \mathbf{x}) p(\mathbf{x})). \end{aligned} \quad (8)$$

Apart from the first term, which is irrelevant when λ is fixed, we note that the objective above promotes q_ψ that minimize (on average) the absolute values of the N residuals considered while simultaneously minimizing the KL-divergence from the prior density adopted.

Remarks:

- The KL-divergence term in Equation (8) can be thought of as a regularization or penalty term, which nevertheless arises naturally in the Bayesian framework adopted. In other physics-informed schemes that have been proposed [43, 57, 54], ad-hoc parameters are generally selected as relative weights of these two terms [58]. Similarly, alternative forms of virtual likelihoods can give rise to the exact expressions found in competitive schemes. E.g. the use of a Gaussian likelihood would yield the sum of the *squares* of the N residuals in the ELBO.
- Furthermore such schemes generally employ collocation-type residuals in the physics-informed term [59, 18, 43], which in our formulation arise as a special case when the weight functions considered take the form of Dirac-deltas i.e. $w_j(s) = \delta(s - s_j)$ where s_j correspond to the collocation points.
- More importantly, by finding the optimal q_ψ we obtain a *probabilistic surrogate* that is capable of providing probabilistic predictions of the solution \mathbf{y} for any input \mathbf{x} . Since the form of q_ψ is critical to the accuracy of the proposed scheme we defer detailed discussions to Section 2.4. As a final note we mention that if a degenerate q_ψ is selected in the form of a Dirac-delta, then one obtains a *deterministic* surrogate as is the majority of the ones proposed in the literature [60, 11, 25].

The evaluation and, more importantly, the maximization of the ELBO $\mathcal{F}(\psi)$ requires the computation of the expectations with respect to q_ψ of the absolute values of the N weighted-residuals appearing in the virtual likelihood. We note that the evaluation of a weighted residual involves the computation of an integral over the problem domain (see e.g. Equation (4)) but not the solution of the PDE. These integrations can be carried out using deterministic or (quasi) Monte-Carlo-based numerical integration schemes [61, 62]. Furthermore, if the weight functions have support on a subset of the problem domain Ω , additional efficiencies can be achieved in the numerical integration.

Independently of the particulars, it is readily understood that as N increases, so does the information we extract from the governing PDE, but so does also the computational effort. In order to improve the computational efficiency of these updates, we propose a Monte Carlo approximation of the pertinent term in the ELBO in Equation (8). In particular

$$\sum_{j=1}^N \langle |r_{w_j}(\mathbf{y}, \mathbf{x})| \rangle_{q_\psi(\mathbf{x}, \mathbf{y})} \approx \frac{N}{M} \sum_{m=1}^M \langle |r_{w_{j_m}}(\mathbf{y}, \mathbf{x})| \rangle_{q_\psi(\mathbf{x}, \mathbf{y})}, \text{ where } j_m \sim \text{Cat}\left(N, \frac{1}{N}\right). \quad (9)$$

In essence, we sample at random and with equal probability $M < N$ weight functions out of the N and use them to approximate the sum. The specifics for the set of N weight functions, which is subsampled, are described in subsection 4.1. As M increases, so does the Monte Carlo error decrease, but so does the computational effort increase. Since the Monte Carlo estimator is unbiased even for $M = 1$, evaluating a single residual is sufficient to guarantee convergence (see Algorithm 1).

In combination with Equation (8) (we omit the first term, which is independent of ψ), this yields the following Monte Carlo approximation to the ELBO:

$$\mathcal{F}(\psi) \approx -\lambda \frac{N}{M} \sum_{m=1}^M \langle |r_{w_{j_m}}(\mathbf{y}, \mathbf{x})| \rangle_{q_\psi(\mathbf{x}, \mathbf{y})} + \left\langle \log \frac{p(\mathbf{y}|\mathbf{x})p(\mathbf{x})}{q_\psi(\mathbf{x}, \mathbf{y})} \right\rangle_{q_\psi(\mathbf{x}, \mathbf{y})} \text{ where } j_m \sim \text{Cat}\left(N, \frac{1}{N}\right). \quad (10)$$

We discuss in subsection 2.4 and in more detail in C how gradients of \mathcal{F} can be computed and used in order to carry out the ELBO maximization. We also note that if a parameterized prior, say $p_\theta(\mathbf{y}|\mathbf{x})$ were to be adopted, then the optimal θ could also be identified by maximizing the corresponding ELBO [21]. While such structured or informative priors could be highly beneficial in accelerating inference and improving predictive accuracy, they are not explored in this paper.

Finally, we note that even though the method described above for subsampling weighting functions and residuals is simple and efficient, other more intelligent procedures could lead to weighting functions of superior informational content. One such idea would be to start with a null set of residuals (i.e. the prior) and successively add one residual at a time (i.e. selecting a new w) based e.g. on maximizing the KL-divergence between the current posterior (or its approximation) and the posterior with the additional residual.

Another scheme could involve the parameterization of w (e.g. by some parameters ϕ) and, subsequently, the iterative maximization of the ELBO w.r.t the parameters ψ followed by a minimization of the ELBO w.r.t. the parameters ϕ for every optimization cycle (i.e. a saddle-point search). We defer a more thorough investigation of these possibilities as well as their effect in reducing the computational effort for future work.

2.4 Form of the Approximating Density q_ψ and Implicit Solvers

In selecting the form of q_ψ and without loss of generality we postulate:

$$q_\psi(\mathbf{x}, \mathbf{y}) = q_\psi(\mathbf{y}|\mathbf{x})q(\mathbf{x}) = q_\psi(\mathbf{y}|\mathbf{x})p(\mathbf{x}) \quad (11)$$

i.e. we use the given density of the parametric input and attempt to approximate the input-to-output map with $q_\psi(\mathbf{y}|\mathbf{x})$ where ψ denotes the tunable parameters. We note that alternate decompositions might be advisable in the context of inverse problems but are not discussed in this work. We note also that a deterministic formulation can be readily adopted by selecting a degenerate density in the form of a Dirac-delta, i.e.:

$$q_\psi(\mathbf{y}|\mathbf{x}) = \delta(\mathbf{y} - \boldsymbol{\mu}_\psi(\mathbf{x})). \quad (12)$$

The sought function $\boldsymbol{\mu}_\psi(\mathbf{x})$ in this case can take the form of *any* of the proposed NN-based architectures such as Fully Connected Neural Networks (FCNNs), Convolutional Neural Networks (CNNs) [20], Deep Neural Operators (DeepONets) [11], Graph Neural Operators (GNOs) [12] or Fourier Neural Operators (FNOs) [42], in which case ψ would correspond to the associated NN-parameters.

While all these architectures have produced good results in a variety of problems, it is easily understood that as the variability and the dimension of the input \mathbf{x} (as well as of the sought output \mathbf{y}) increase, so must the complexity of the aforementioned NN-based schemes increase. At a practical level, it is not uncommon that one must train for millions or billions of parameters ψ ([20, 11, 18]). This situation is much more pronounced in *multiscale* problems which are discussed in Section 3 where input and output de facto imply very high-dimensional representations.

More importantly, as such interpolators are agnostic of the physical context, they face significant problems in generalizing [11, 13]. For example, if out-of-distribution predictions are sought for a significantly different input \mathbf{x} as compared to the ones used in training, then the predictive accuracy can significantly drop [18]. In addition, and in the context of PDEs in particular, if one were to seek predictions under a different set of boundary conditions than the ones employed during training, most likely, these predictions would be significantly off and by a large margin (see Section 4).

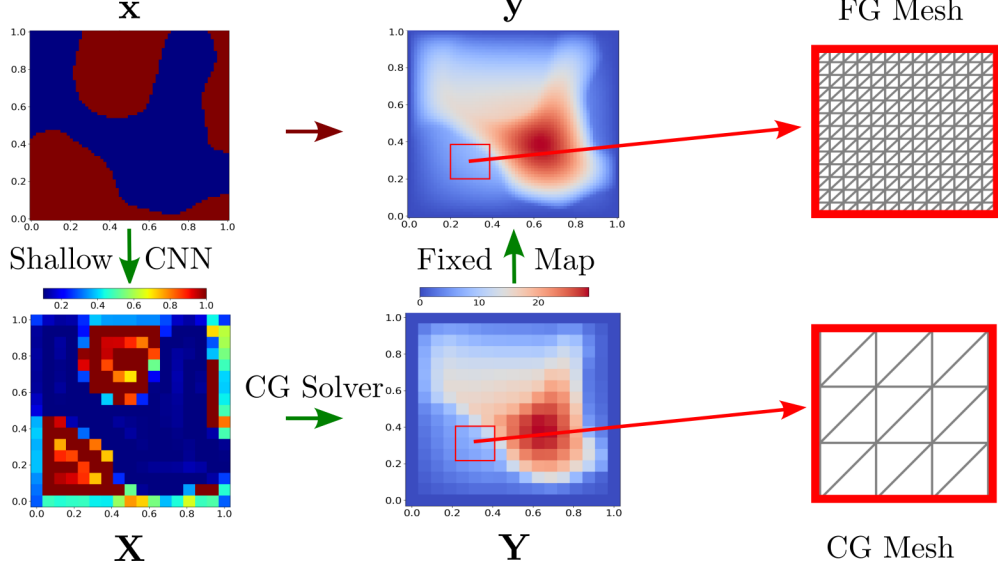


Figure 1: Schematic illustration of the proposed, physics-aware architecture for parametrizing the mean solution $\mu_\psi(\mathbf{x})$ as described in subsection 2.4.

One could claim that enlarged datasets, bigger models, or progress in pertinent hardware could alleviate or overcome these difficulties. Nevertheless, none of these strategies addresses the fundamental, underlying question which is how to find the requisite information bottlenecks that lead to drastic dimensionality reductions and lightweight surrogates and how to achieve this in a problem-aware manner that is capable of producing accurate predictions under extrapolative settings [49].

In view of these objectives and following previous work [49, 21], we propose incorporating coarse-grained (CG) versions of the governing PDE as an implicit solver [63, 64] in the surrogate constructed. We elaborate on this in the subsequent sections, and more importantly, we extend it to *multiscale* problems, which pose a unique set of challenges.

For the purposes of the Variational Inference proposed, we employ a multivariate Gaussian of the form:

$$q_\psi(\mathbf{y}|\mathbf{x}) = \mathcal{N}(\mathbf{y} | \mu_\psi(\mathbf{x}), \Sigma_\psi) \quad (13)$$

the mean and covariance of which are discussed in the sequel.

In the context of materials problems and as in the model formulation of Equation (3) where the inputs \mathbf{x} parametrize a, potentially multiscale, material property field, we consider a (much) coarser, discretized version (see e.g. Figure 1) of the governing PDE where \mathbf{X}, \mathbf{Y} denote the respective, discretized input and output. By construction, their dimension is much lower as compared to their reference, fine-grained counterparts \mathbf{x}, \mathbf{y} . As such, the solution of the associated (non)linear algebraic equations to obtain the solution \mathbf{Y} for any input \mathbf{X} is much faster. As we have shown in [49], the \mathbf{X} could be thought of as some effective material properties which serve as the requisite information bottleneck to the problem. Furthermore, it is possible that a different (discretized) PDE could be used as a stencil for the coarse-grained model.

We complement the implicit, differentiable, and vectorized, input-output map $\mathbf{Y}(\mathbf{X})$ of the CG model, with two additional components:

- a **fine-to-coarse input map** denoted by $\mathbf{X}_{\psi_x}(\mathbf{x})$ that we express with a shallow CNN parameterized by ψ . This consists merely of 2 to 3 convolution and deconvolution layers, as well as a few, average pooling layers. To improve stability we employ batch normalization wherever is required, while the only kind of activation function used was Softplus. The number of feature maps of each layer is limited, and the number of total trainable parameters is *three orders of magnitude lower* compared to other state-of-the-art models used on the same problems (more details in A).
- a **coarse-to-fine output map** denoted by $\mathbf{y}(\mathbf{Y})$ that attempts to reconstruct the reference, fine-grained (FG) output \mathbf{y} given the CG output \mathbf{Y} . In our illustrations, this map was fixed (i.e. it had no trainable parameters), which has the desirable effect of forcing \mathbf{X} to attain physically meaningful values in the context of materials problems. In particular a *linear map* of the form $\mathbf{y} = \mathbf{A}\mathbf{Y}$ was used where the matrix \mathbf{A} was pre-computed so

Algorithm 1 PANIS Training Algorithm

```
1: Select  $\lambda, N, M$ ; Initialize  $\psi \leftarrow \psi_0$ ;
2: Generate a set of  $N$  weighting functions ▷ see subsection 2.3
3:  $\ell \leftarrow 0$  ▷ Initialize iteration counter
4: while  $\mathcal{F}_\psi$  not converged do
5:   Draw  $M$  weight functions at random out of the  $N$  ▷ see Equation (9)
6:   Draw  $\mathbf{x} \sim p(\mathbf{x})$ 
7:   Generate  $\mathbf{y} \leftarrow \mu_{\psi_x}(\mathbf{x}) + \mathbf{L}_y \varepsilon_1 + \sigma_y \varepsilon_2$ ,  $\varepsilon_1 \sim \mathcal{N}(\mathbf{0}, \mathbf{I}_{d'_y})$ ,  $\varepsilon_2 \sim \mathcal{N}(\mathbf{0}, \mathbf{I}_{d_y})$ 
8:   Approximate  $\mathcal{F}_\psi$  ▷ Monte Carlo Approximation according to Equation (10)
9:   Estimate  $\nabla_{\psi} \mathcal{F}_\psi$  ▷ Backpropagation for estimating  $\nabla_{\psi} \mathcal{F}_\psi$ 
10:   $\psi_{\ell+1} \leftarrow \psi_\ell + \rho^{(\ell)} \odot \nabla_{\psi} \mathcal{F}_\psi$  ▷ SGA using ADAM for determining the learning rate  $\rho^{(\ell)}$ 
11:   $\ell \leftarrow \ell + 1$ 
```

as to minimize the mean-square error in the resulting solution fields (more details in B). A very important benefit of the use of this implicit solver and of the associated map is the direct imposition of boundary conditions on the CG model, i.e. on \mathbf{Y} , which are automatically transferred to \mathbf{y} . In this manner and we demonstrate in the numerical illustrations, our model can generalize under varying boundary conditions.

The composition of these three functions leads to:

$$\mu_\psi(\mathbf{x}) = \mathbf{A} \mathbf{Y}(\mathbf{X}_{\psi_x}(\mathbf{x})). \quad (14)$$

In the formulation employed in the ensuing numerical experiments, the sole trainable parameters are associated with the inner layer i.e. the fine-to-coarse map from \mathbf{x} to \mathbf{X} . More complex formulations involving trainable parameters in the other two layers could be readily accommodated. We note that all three layers are differentiable, and each evaluation requires the solution of the CG model. Differentiation of μ_ψ with respect to ψ_x as needed for training requires a backward pass which can be computed with Automatic Differentiation [65, 66] and/or adjoint formulations of the governing equations of the CG model [67, 68].

With regards to the covariance matrix Σ_ψ in Equation 13 and given the high dimension of \mathbf{y} , we advocate a low-rank approximation of the form:

$$\Sigma_\psi = \mathbf{L}_y \mathbf{L}_y^T + \sigma_y^2 \mathbf{I}_{d_y}, \quad (15)$$

where \mathbf{L}_y is a rectangular matrix of dimension $d_y \times d'_y$ (with $d'_y \ll d_y$) and $\sigma_y^2 \in \mathbb{R}_+$ is a scalar. The first term is responsible for introducing correlation between the solution vector's entries whereas the second term accounts for the residual, global uncertainty in the solution. The low-rank approximation ensures that the number of unknown parameters in \mathbf{L}_y grows *linearly* with the dimension of \mathbf{y} .

In summary, the vector of trainable parameters ψ consists of:

$$\psi = \{\psi_x, \mathbf{L}_y, \sigma_y^2\}. \quad (16)$$

Maximization of the ELBO \mathcal{F} with respect to ψ is carried out in the context of Stochastic Variational Inference (SVI) [69, 55]. This entails Monte Carlo approximations for the intractable expectations appearing in the gradient of $\nabla_{\psi} \mathcal{F}$ and Stochastic Gradient Ascent (SGA). In our experiments, we used ADAM for the SGA because of its adaptive learning rates, momentum-based updates, and its effectiveness as an optimization algorithm [70, 71]. Critical to achieving Monte Carlo estimators with low error is the use of the reparametrization trick [72, 73], which for \mathbf{y} sampled from $q(\mathbf{y}|\mathbf{x})$ implies:

$$\mathbf{y} = \mu_{\psi_x}(\mathbf{x}) + \mathbf{L}_y \varepsilon_1 + \sigma_y \varepsilon_2, \quad \varepsilon_1 \sim \mathcal{N}(\mathbf{0}, \mathbf{I}_{d'_y}), \quad \varepsilon_2 \sim \mathcal{N}(\mathbf{0}, \mathbf{I}_{d_y}), \quad (17)$$

where $\dim(\varepsilon_1) = d'_y$, $\dim(\varepsilon_2) = d_y$. In Algorithm 1 we summarize the main algorithmic steps.

2.5 PANIS - Posterior Predictive Estimates

Upon convergence of the aforementioned SVI scheme and the identification of the optimal ψ parameters, the approximate posterior $q_\psi(\mathbf{y}|\mathbf{x})$ in Equation (13) can be used for posterior predictive estimates. For each test input \mathbf{x} , samples

Algorithm 2 Posterior Predictive Estimates for the solution (Equation (2)) for a test input \mathbf{x} .

- | | |
|--|---|
| 1: Compute $u_\mu(\mathbf{s}) \leftarrow \sum_{i=1}^{N_\eta} \mu_{\psi}(\mathbf{x})_i \eta_i(\mathbf{s})$ | ▷ Posterior Mean of Solution Field ; |
| 2: Compute $u_\sigma(\mathbf{s}) \leftarrow \sqrt{\sum_{i,j=1}^{N_\eta} \eta_i(\mathbf{s}) \Sigma_{\psi,ij} \eta_j(\mathbf{s})}$ | ▷ Posterior St. Deviation of Solution Field |
| 3: $u_U(\mathbf{s}) \leftarrow u_\mu(\mathbf{s}) + 2u_\sigma(\mathbf{s})$ | ▷ Upper Uncertainty Bound Field |
| 4: $u_L(\mathbf{s}) \leftarrow u_\mu(\mathbf{s}) - 2u_\sigma(\mathbf{s})$ | ▷ Lower Uncertainty Bound Field |
-

from $q_\psi(\mathbf{y}|\mathbf{x})$ can readily be drawn as in Equation (17). We note that for each such sample, the solution of the CG model (i.e. the computation of \mathbf{Y} for the corresponding $\mathbf{X}_{\psi_x}(\mathbf{x})$) would be required. For the representation of $u_{\mathbf{y}}$ in Equation (2) (which is linear with respect to \mathbf{y}) posterior predictive estimates of the continuous PDE-solution $u_{\mathbf{y}}(\mathbf{s})$ can be readily obtained as detailed in Algorithm 2 by making use of $\mu_\psi(\mathbf{x})$ in (14) and Σ_ψ in (15).

In order to comparatively assess the performance of the proposed framework, for each of the problems in the numerical illustrations we consider a validation dataset $\mathcal{D}_v = \{\mathbf{x}^{(j)}, \mathbf{u}^{(j)}\}_{j=1}^{N_v}$ consisting of N_v input-solution pairs, which were obtained by using a conventional FEM solver on a fine mesh. Each vector $\mathbf{u}^{(j)}$ refers to the discretized version of $u^{(j)}(\mathbf{s})$, the specifics of which are described in Section 4. The following metrics were computed:

Coefficient of Determination R^2 : The coefficient of determination is a widely used metric [74] to quantify the accuracy of point estimates, and it is defined as follows

$$R^2 = 1 - \frac{\sum_{j=1}^{N_j} \|\mathbf{u}^{(j)} - \mathbf{u}_\mu^{(j)}\|_2^2}{\sum_{j=1}^{N_j} \|\mathbf{u}^{(j)} - \bar{\mathbf{u}}^{(j)}\|_2^2}, \quad (18)$$

where $\mathbf{u}_\mu^{(j)}$ is the mean discretized solution field as predicted from the predictive posterior of our trained model for each $\mathbf{x}^{(j)}$ in \mathcal{D}_v , $\bar{\mathbf{u}}^{(j)} = \frac{1}{N_j} \sum_{j=1}^{N_j} \mathbf{u}^{(j)}$ is the sample mean over the validation dataset and $\|\cdot\|_2$ denotes the L_2 -norm over the problem domain Ω . The maximum score is $R^2 = 1$, which is attained when the predictive mean estimates coincide with the true solutions. It is noted that negative R^2 values are also valid since the second term is merely weighted (not bounded) by the empirical variance of the validation dataset.

Relative L_2 Error ϵ : The relative L_2 error is commonly used as an evaluation metric for comparisons between state-of-the-art surrogate models for stochastic PDEs [20, 75, 18]. It is defined as:

$$\epsilon = \frac{1}{N_j} \sum_{j=1}^{N_j} \frac{\|\mathbf{u}^{(j)} - \mathbf{u}_\mu^{(j)}\|_2}{\|\mathbf{u}^{(j)}\|_2}. \quad (19)$$

The overwhelming majority of competitive methods produce deterministic predictions, i.e. point estimates, which prevent a direct comparison with the predictive posterior $q_\psi(\mathbf{y}|\mathbf{x})$ obtained by our framework. Nevertheless, in the illustrations of Section 4, we report upper/lower posterior uncertainty bounds obtained as detailed in Algorithm 2.

3 Learning solutions to multiscale PDEs

As mentioned in section 1, a challenging case in which data-driven (physics-informed or not) methods struggle, are multiscale problems. In the context of heterogeneous media such problems naturally arise as the scale of variability of the underlying microstructure becomes smaller. Capturing this would, in general, require very high-dimensional input \mathbf{x} and output \mathbf{y} vectors, and while existing neural architectures could be employed without alterations, they would require bigger and deeper nets (i.e. more trainable parameters) as well as, in general, more training data. In multiscale PDEs, we are interested in finding an effective or homogenized model that captures the macroscale components of the solution. Classical homogenization techniques rely on very special features such as periodicity at the fine-scale [1]. Several numerical homogenization techniques [76] have been developed which consistently upscale fine-scale information which, although small in magnitude, can have a significant effect in the macroscale solution [77]. In the context of weighted residuals, setting these fine-scale components of the solution to zero would lead to significant errors in the coarse-scale components [78, 79].

While several data-driven strategies have been proposed for learning such effective models [80, 81, 82, 83], to the best of our knowledge all these rely on labeled data i.e. pairs of inputs \mathbf{x} and outputs/solutions \mathbf{y} of the multiscale PDE. In

the following, we propose **multiscale PANIS** (mPANIS), which is an extension of the previously described framework that can learn such effective models *without* ever solving the multiscale PDE but solely by computing weighted residuals (and their derivatives). The enabling component remains the physics-aware, implicit solver at the core of our surrogate, which can be learned by a small number of inputs and corresponding residuals.

3.1 Model extension for multiscale PDEs (mPANIS)

We additively decompose the solution-output \mathbf{y} as:

$$\mathbf{y} = \mathbf{y}_c + \mathbf{y}_f, \quad (20)$$

where \mathbf{y}_c accounts for the coarse-scale features we are interested in and \mathbf{y}_f for the fine-scale fluctuations that are not of interest. In the context of the probabilistic models advocated, such a task would entail learning $q_\psi(\mathbf{y}_c|\mathbf{x})$, and $q_\psi(\mathbf{y}_f|\mathbf{x})$. On the basis of the previous single-scale model, we employ a $q_\psi(\mathbf{y}_c|\mathbf{x})$ of the form:

$$q_\psi(\mathbf{y}_c|\mathbf{x}) = \mathcal{N}(\mathbf{y}_c|\boldsymbol{\mu}_\psi(\mathbf{x}), \boldsymbol{\Sigma}_\psi), \quad (21)$$

where as in Equation (14) we make use of the implicit solver and the associated fine-to-coarse $\mathbf{X}_{\psi_x}(\mathbf{x})$ and coarse-to-fine $\mathbf{A}\mathbf{Y}$ (see section 2.4) maps such that $\boldsymbol{\mu}_\psi(\mathbf{x}) = \mathbf{A}\mathbf{Y}(\mathbf{X}_{\psi_x}(\mathbf{x}))$. Hence, the mean of \mathbf{y}_c lives on the subspace spanned by the columns of the \mathbf{A} matrix, and its reduced coordinates are determined by the output \mathbf{Y} of the implicit solver. We also introduce a learnable correlation on this subspace by adopting a $d_y \times d_y$ covariance matrix $\boldsymbol{\Sigma}_\psi = \mathbf{A}\mathbf{S}_\psi\mathbf{A}^T$ where the inner $d_Y \times d_Y$ covariance matrix \mathbf{S}_ψ is:

$$\mathbf{S}_\psi = \mathbf{L}_Y\mathbf{L}_Y^T + \sigma_Y^2\mathbf{I}_{d_Y}. \quad (22)$$

The rectangular matrix \mathbf{L}_Y of dimension $d_Y \times d'_Y$ (with $d'_Y < d_Y$) captures the principal directions where correlation appears and the scalar $\sigma_Y \in \mathbb{R}_+$ the residual uncertainty. We emphasize that in this manner, the posterior uncertainty for \mathbf{y}_c will be concentrated in the subspace spanned by the columns of the \mathbf{A} matrix.

Given the aforementioned representation of \mathbf{y}_c , the fine-scale features \mathbf{y}_f in Equation (20) are expressed as:

$$\mathbf{y}_f = \mathbf{A}_\perp\mathbf{y}'_f, \quad (23)$$

where the columns of matrix \mathbf{A}_\perp span the orthogonal complement of the subspace spanned by the columns of \mathbf{A} above. This matrix can be readily computed, and its use ensures that the \mathbf{y}_f complements \mathbf{y}_c in representing the solution \mathbf{y} . Given the very high dimension of \mathbf{y}'_f , which is commensurate with that of the full solution \mathbf{y} and which would pose significant, if not insurmountable, challenges in learning $q_\psi(\mathbf{y}'_f|\mathbf{x})$, we propose the following form which is justified by the ability of the \mathbf{y}_c -part of the model to learn from very few inputs \mathbf{x} .

In particular, consider an empirical approximation of the input density $p(\mathbf{x})$ consisting of K samples, i.e.:

$$p(\mathbf{x}) = \frac{1}{K} \sum_{k=1}^K \delta(\mathbf{x} - \mathbf{x}_k). \quad (24)$$

We propose employing an approximate posterior:

$$q_\psi(\mathbf{y}'_f|\mathbf{x}_k) = \delta(\mathbf{y}'_f - \mathbf{y}'_{f,k}). \quad (25)$$

This implies that for each atom \mathbf{x}_k in Equation (24), we make use of a distinct Dirac-delta, centered at an (unknown) $\mathbf{y}'_{f,k}$. The corresponding $\{\mathbf{y}'_{f,k}\}_{k=1}^K$ become part of the vector of the unknown parameters ψ which are determined by maximizing the ELBO. While the dimension of each $\mathbf{y}'_{f,k}$ can be high, the number K of \mathbf{x}_k -samples can be small due to the capacity of the proposed model architecture to learn from small data. In summary, the vector of parameters ψ that would need to be found by maximizing the corresponding ELBO (see subsequent section) in the multiscale version of our framework consists of:

$$\psi = \{\psi_x, \mathbf{L}_Y, \sigma_Y^2, \{\mathbf{y}'_{f,k}\}_{k=1}^K\}. \quad (26)$$

3.2 Algorithmic implementation

Given the representation of the solution \mathbf{y} as in Equation (20), the latent variables to be inferred in the Variational Inference framework advocated are now \mathbf{y}_c and \mathbf{y}'_f (Equation (23)). The associated weighted residuals, which are used

as virtual observables, can be readily re-expressed with respect to \mathbf{y}_c and \mathbf{y}'_f as $\{r_{w_j}(\mathbf{y}_c, \mathbf{y}'_f, \mathbf{x})\}_{j=1}^N$. In combination with priors $p(\mathbf{y}_c|\mathbf{x})$, $p(\mathbf{y}'_f|\mathbf{x})$ ⁴, we obtain analogously to Equation (8) the following ELBO⁵:

$$\mathcal{F}(\psi) = -\lambda \sum_{j=1}^N \langle |r_{w_j}(\mathbf{y}_c, \mathbf{y}'_f, \mathbf{x})| \rangle_{q_\psi(\mathbf{x}, \mathbf{y}_c, \mathbf{y}'_f)} + \left\langle \log \frac{p(\mathbf{y}_c|\mathbf{x})p(\mathbf{y}'_f|\mathbf{x})p(\mathbf{x})}{q_\psi(\mathbf{x}, \mathbf{y}_c, \mathbf{y}'_f)} \right\rangle_{q_\psi(\mathbf{x}, \mathbf{y}_c, \mathbf{y}'_f)}. \quad (27)$$

The particular form of $q_\psi(\mathbf{y}'_f|\mathbf{x})$ in Equation (25) in combination with the empirical approximation of $p(\mathbf{x})$ in Equation (24) yield the following result for the first term in the ELBO:

$$\sum_{j=1}^N \langle |r_{w_j}(\mathbf{y}_c, \mathbf{y}'_f, \mathbf{x})| \rangle_{q_\psi(\mathbf{x}, \mathbf{y}_c, \mathbf{y}'_f)} = \frac{1}{K} \sum_{k=1}^K \sum_{j=1}^N \langle |r_{w_j}(\mathbf{y}_c, \mathbf{y}'_{f,k}, \mathbf{x}_k)| \rangle_{q_\psi(\mathbf{y}_c|\mathbf{x})}. \quad (28)$$

This lends itself naturally to Monte Carlo approximations both in terms of the index k (i.e. by subsampling only a subset of the K atoms \mathbf{x}_k in Equation (24)) as well as in terms of the index j i.e. over the considered residuals as explained in Equation (9). Expectations with respect to $q(\mathbf{y}_c|\mathbf{x})$ are also approximated by Monte Carlo in combination with the reparametrization trick [72, 73], which according to Equation (21) can make use of \mathbf{y}_c samples generated as follows:

$$\mathbf{y}_c = \mathbf{A} \left(\mathbf{Y} \left(\mathbf{X}_{\psi_x}(\mathbf{x}) + \mathbf{L}_Y \varepsilon_1 + \sigma_Y \varepsilon_2 \right) \right), \quad \varepsilon_1 \sim \mathcal{N}(\mathbf{0}, \mathbf{I}_{d_Y}), \quad \varepsilon_2 \sim \mathcal{N}(\mathbf{0}, \mathbf{I}_{d_Y}), \quad (29)$$

where $\dim(\varepsilon_1) = d'_Y$, $\dim(\varepsilon_2) = d_Y$. Details about the ELBO and the computation of its gradient with respect to ψ are contained in C. In Algorithm 3, we summarize the basic steps involved.

Remarks:

- One of the common issues in pertinent formulations is the enforcement of Dirichlet boundary conditions [20]. In our framework, these could be enforced a priori in \mathbf{y} , although depending on the representation of the solution, this is not always straightforward. A more elegant strategy would be to introduce the BCs at certain boundary points as actual observables through an additional likelihood (e.g. a Gaussian) which would ensure that the posterior on \mathbf{y} satisfies them (up to some prescribed precision). The disadvantage of both of these procedures is that the approximate posterior, either $q_\psi(\mathbf{y}|\mathbf{x})$ or $q_\psi(\mathbf{y}_c|\mathbf{x})$ will also (approximately at least) enforce these Dirichlet BCs. Hence it would be useless in predictive settings where the PDE is the same but the Dirichlet BCs are different. In our formulation, Dirichlet BCs are enforced at the level of the implicit solver (i.e. on \mathbf{Y}) and are transferred to \mathbf{y} through the appropriately fine-tuned linear map $\mathbf{y} = \mathbf{A} \mathbf{Y}$ (see B). In the multiscale setting where \mathbf{y}_c inherits these Dirichlet BCs as described above, we set the corresponding \mathbf{y}_f (or \mathbf{y}'_f in Equation (23)) equal to 0 a priori. As we demonstrate in the numerical illustrations, this enables us to produce extremely accurate predictions under BCs *not encountered* during training.
- The hyperparameter λ appearing in the ELBO and which controls the tightness of the tube that is implicitly defined in the joint (\mathbf{x}, \mathbf{y}) space around the 0 residual manifold, offers a natural way to temper computations. One can envision starting with a small λ , which would correspond to an easier posterior to approximate as the residuals could be far from 0 (in the limit that $\lambda = 0$, the posterior coincides with the prior). Subsequently, this could be, potentially adaptively, increased until the target value is reached in order to attain posteriors (and approximations thereof) that are more tightly concentrated around the solution manifold. We defer investigations in this direction to future work.
- Adaptive learning strategies could also be employed in terms of the samples $\{\mathbf{x}_k\}_{k=1}^K$ employed during training. This is especially important in the multiscale setting as the dimension of the parameters $\{\mathbf{y}'_{f,k}\}_{k=1}^K$ that need to be fine-tuned is proportional to K . We defer investigations along this direction to future work.

3.3 mPANIS - Posterior Predictive Estimates

Upon convergence of the aforementioned SVI scheme and the identification of the optimal ψ parameters, the approximate posterior $q_\psi(\mathbf{y}_c|\mathbf{x})$ in Equation (21), i.e. the one accounting for the coarse-scale features of the full solution, can be used for posterior predictive estimates. For each test \mathbf{x} , samples from $q_\psi(\mathbf{y}_c|\mathbf{x})$ can readily be drawn as in Equation (29). We note that for each such sample, the solution of the CG model (i.e. the determination of \mathbf{Y} for the corresponding $\mathbf{X}_{\psi_x}(\mathbf{x})$) would be required.

⁴As in the single-scale case, uninformative priors were used here in the form of $\mathcal{N}(\mathbf{0}, \sigma^2 \mathbf{I})$, where $\sigma^2 = 10^{16}$

⁵We omit any constant terms

Algorithm 3 mPANIS Training Algorithm.

A set of random, fixed to the number inputs $\mathbf{x}_k = \{\mathbf{x}_1, \mathbf{x}_2, \dots, \mathbf{x}_K\}$ is given:

- 1: Select λ, N, M ; Initialize $\psi \leftarrow \psi_0$;
 - 2: Construct a set of N weighting functions ▷ see subsection 2.3
 - 3: $\ell \leftarrow 0$ ▷ Initialize iteration counter
 - 4: **while** \mathcal{F}_ψ not converged **do**
 - 5: Draw M weight functions at random ▷ see Equation (9)
 - 6: Draw a subset of the K atoms $\mathbf{x}_k: \mathbf{x}_{k_s} \sim p(\mathbf{x}), k_s < K$ ▷ see Equation (24)
 - 7: Generate $\mathbf{y}_{c,k_s} \leftarrow \mathbf{A} (\mathbf{Y} (\mathbf{X}_{\psi_x}(\mathbf{x}_{k_s}) + \mathbf{L}_Y \varepsilon_1 + \sigma_Y \varepsilon_2))$, $\varepsilon_1 \sim \mathcal{N}(\mathbf{0}, \mathbf{I}_{d_Y'})$, $\varepsilon_2 \sim \mathcal{N}(\mathbf{0}, \mathbf{I}_{d_Y})$
 - 8: $\mathbf{y} \leftarrow \mathbf{y}_{c,k_s} + \mathbf{A}_\perp \mathbf{y}'_{f,k_s}$
 - 9: Approximate \mathcal{F}_ψ ▷ **Monte Carlo** Approximation according to Equation (27)
 - 10: Estimate $\nabla_\psi \mathcal{F}_\psi$ ▷ **Backpropagation** for estimating $\nabla_\psi \mathcal{F}_\psi$
 - 11: $\psi_{\ell+1} \leftarrow \psi_\ell + \rho^{(\ell)} \odot \nabla_\psi \mathcal{F}_\psi$ ▷ **SGA** using **ADAM** for determining the learning rate $\rho^{(\ell)}$
 - 12: $\ell \leftarrow \ell + 1$
-

Algorithm 4 mPANIS Posterior Predictive Estimates for coarse-scale solution (Equation (2)) for a test input \mathbf{x}

- 1: Compute $u_{c,\mu}(\mathbf{s}) \leftarrow \sum_{i=1}^{N_\eta} (\mathbf{A} (\mathbf{Y} (\mathbf{X}_{\psi_x}(\mathbf{x})))_i \eta_i(\mathbf{s})$ ▷ Posterior Mean of Solution Field ;
 - 2: Compute $u_{c,\sigma}(\mathbf{s}) \leftarrow \sqrt{\sum_{i,j=1}^{N_\eta} \eta_i(\mathbf{s}) \Sigma_{\psi,i,j} \eta_j(\mathbf{s})}$ ▷ Posterior St. Deviation of Solution Field
 - 3: $u_{c,U}(\mathbf{s}) \leftarrow u_{c,\mu}(\mathbf{s}) + 2u_{c,\sigma}(\mathbf{s})$ ▷ Upper Uncertainty Bound Field
 - 4: $u_{c,L}(\mathbf{s}) \leftarrow u_{c,\mu}(\mathbf{s}) - 2u_{c,\sigma}(\mathbf{s})$ ▷ Lower Uncertainty Bound Field
-

In order to comparatively assess the performance of the proposed framework in the context of multiscale problems, we consider a validation dataset $\mathcal{D}_v = \{\mathbf{x}^j, \mathbf{u}^j\}_{j=1}^{N_v}$ consisting of N_v inputs and discrete solution pairs, which were obtained by using a conventional FEM solver on a fine mesh. From these we extract the coarse-scale part $\mathbf{u}_c^j = \sum_i^{d_y} y_{c,i}^j \eta_i$ of each \mathbf{u}^j by projecting on the subspace spanned by the columns of the \mathbf{A} matrix (i.e. $\mathbf{y}_c^j = (\mathbf{A}^T \mathbf{A})^{-1} \mathbf{A}^T \mathbf{y}^j$), where η_i are the discretized equivalent of the shape functions described in Equation (2).

However, this is sufficient to approximate the solution well enough since proper uncertainty bounds will quantify the error. The detailed process for making predictions in the multiscale setup is shown in Algorithm 4. Other than neglecting the influence of the fine-scale part, the procedure and the validation metrics are identical to the ones described in Section 2.5.

4 Numerical Illustrations

This section contains several numerical illustrations of the performance of the proposed (m)PANIS framework on linear and nonlinear PDEs. It is compared with the state-of-the-art method of Physics Informed Fourier Neural Operators (PINO) [43]. In parallel, components of the model generically described in the previous sections are specified, and additional implementation details are provided. Our objectives are to illustrate:

- the comparative performance under varying dimensions of the parametric input (**predictive accuracy**).
- the very low number of training parameters of the proposed architectures in relation to competitors (**lightweight**).
- the ability of the proposed framework to generalize i.e. to provide accurate predictions in out-of-distribution settings as well as under different boundary conditions (**generalization**).
- the ability to capture the low-frequency components of the solution in multiscale PDEs (**multiscale**).

The general implementation of PANIS and the dedicated coarse-grained solver mentioned in subsection 2.4 is based on PyTorch [84]. Training was conducted on an H100 Nvidia GPU and takes ~ 10 min for the ELBO to converge (see Figure 2) in the case of PANIS and ~ 2195 min in the case of PINO. The validation dataset in all the subsequent illustrations consists of $N_v = 100$ input-solution pairs. Reference solutions were obtained using Fenics [85] and a uniform, finite element mesh with 57600 nodal points.

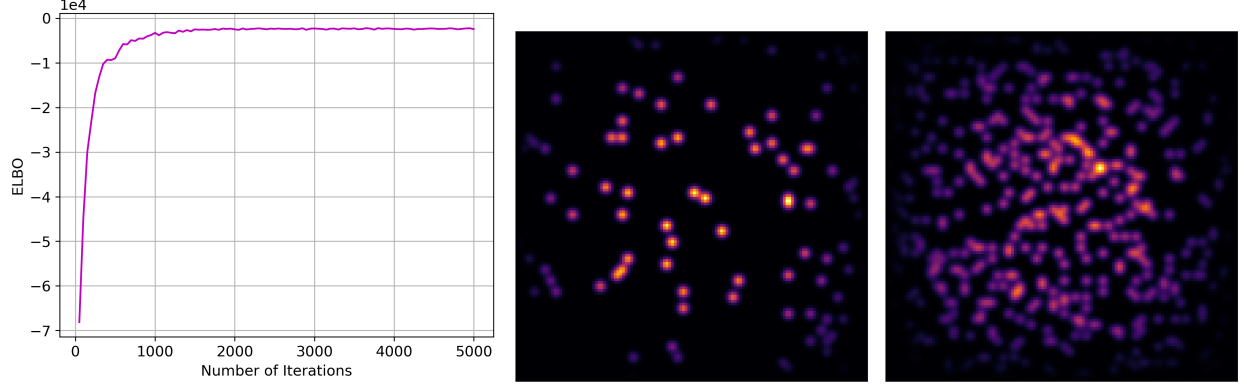


Figure 2: Convergence of the ELBO \mathcal{F} for PANIS, when trained on microstructures with $VF = 50\%$ and BCs $u_0 = 0$ (left). Illustration of 100 and 500 randomly selected RBF-based weight functions w_j according to algorithm 1 (middle-right). Each one of these w_j 's corresponds to a single weighted residual.

A github repository containing the associated code and illustrative examples will become available upon publication at <https://github.com/pkmtum/PANIS>.

4.1 High Dimensional Darcy Problem

We begin with the Darcy flow equation:

$$\begin{aligned} \nabla \cdot (-c(\mathbf{s}; \mathbf{x}) \nabla u(\mathbf{s})) &= f, \quad \mathbf{s} \in \Omega = [0, 1] \times [0, 1] \\ u(\mathbf{s}) &= u_0, \quad \mathbf{s} \in \Gamma_D \end{aligned} \quad (30)$$

as this PDE has been considered by the majority of state-of-the-art methods [13] [43] [75] and the respective code is generally available for producing the following comparative results. In the following, we assume that $f = 100$, $u_0 = 0$, and the input \mathbf{x} parametrizes the permeability field $c(\mathbf{s}; \mathbf{x})$ as described in the sequel.

Input permeability $c(\mathbf{s}; \mathbf{x})$: The permeability fields are generated as cut-offs from an underlying Gaussian field. In particular we consider a zero-mean Gaussian field $G(\mathbf{s}; \mathbf{x}) = \sum_{i=1}^{d_x} \sqrt{\lambda_i} x_i v_i(\mathbf{s})$, where $x_i \sim \mathcal{N}(0, 1)$ determine the input vector \mathbf{x} , λ_i are the eigenvalues and $v_i(\mathbf{s})$ the eigenfunctions of the covariance kernel $k(\mathbf{s}, \mathbf{s}') = \exp\left(-\frac{\|\mathbf{s} - \mathbf{s}'\|_2^2}{l^2}\right)$ where l determines the length scale [20]. By controlling the numbers of terms d_x , we can control the dimension of the parametric input. We generate $c(\mathbf{s}; \mathbf{x})$ corresponding to a binary medium as follows:

$$c(s_i, \mathbf{x}) = \begin{cases} 1, & \text{if } G(s_i; \mathbf{x}) \geq t \quad (\text{phase 1}) \\ \frac{1}{CR}, & \text{if } G(s_i; \mathbf{x}) < t \quad (\text{phase 2}) \end{cases} \quad (31)$$

where the cut-off threshold is set as $t = \Phi^{-1}(VF)$ where VF is the prescribed volume fraction of phase 1 and Φ is the standard Gaussian CDF (e.g. for $VF = 0.5$, $t = 0$). The parameter CR defines the contrast ratio in the properties of the phases, which has a significant impact on the medium's response as well as on the construction of pertinent surrogates. In general, the higher CR is, the more higher-order statistics affect the response [1]. We employed a $CR = 10$ in the subsequent illustrations, although much smaller values are generally selected [75, 86].

As mentioned in subsection 2.4, the first layer of PANIS architecture (see Equation (14)) involves the fine-to-coarse map denoted by $\mathbf{X}_{\psi_x}(\mathbf{x})$ that is realized as a shallow CNN (Appendix A). We note at this point that the input of the CNN is the conductivity field $c(\mathbf{s}; \mathbf{x})$ (i.e. implicitly \mathbf{x}) obtained from Equation (31) and the output are the effective properties \mathbf{X} . Some intuition about the role of $c(\mathbf{s}; \mathbf{x})$ and \mathbf{X} could be drawn from Figure 3, which visualizes some indicative pairs of $c(\mathbf{s}; \mathbf{x})$ and \mathbf{X} . For each full conductivity field $c(\mathbf{s}; \mathbf{x})$, the model learns a coarse-grained equivalent \mathbf{X} , which, when combined with the rest of the model components, scores best in terms of the weighted residuals. In general, areas with high/low $c(\mathbf{s}; \mathbf{x})$ yield areas with high/low \mathbf{X} -values respectively, although the ranges can differ.

Trial solutions and weighting functions: The solution u is represented as in Equation (2) with:

$$\eta_i(\mathbf{s}) = \exp\left(\frac{\|\mathbf{s} - \mathbf{s}_{i,0}\|_2^2}{\Delta l^2}\right) \quad (32)$$

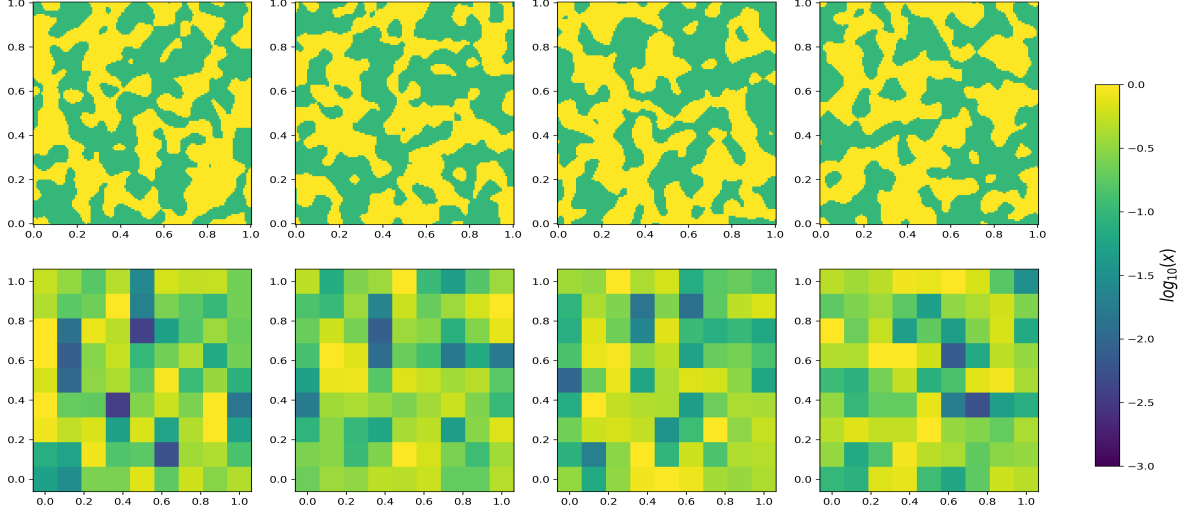


Figure 3: Indicative pairs of the full permeability field $c(\mathbf{s}; \mathbf{x})$ (generated for $l = 0.05$ as described in section ??) and the learned coarse-grained input \mathbf{X} .

In total, $d_{\mathbf{y}} = 4096$ (i.e. $\dim(\mathbf{y}) = 4096$) functions were used. The center-points $\mathbf{s}_{i,0}$ were located on a regular 64×64 grid over the problem domain. As mentioned earlier, BCs are enforced indirectly through the implicit solver (i.e. through \mathbf{Y} in Equation (14)).

For the population of N weighting functions $w_j(\mathbf{s})$ that define the corresponding weighted residuals in Equation (5), the same functions $\eta_j(\mathbf{s})$ above were employed with the following differences for PANIS and mPANIS:

- For PANIS, $N = 289$ and the center-points $\mathbf{s}_{i,0}$ were located on a regular grid 17×17 .
- For mPANIS, $N = 4096$ and the center-points $\mathbf{s}_{i,0}$ were located on a regular grid 64×64 .

These were multiplied with the function $\tau(\mathbf{s}) = s_1(1 - s_1) s_2(1 - s_2)$, which is merely used to enforce that they are zero on the Dirichlet boundary⁶, i.e.:

$$w_j(\mathbf{s}) = \tau(\mathbf{s}) \eta_j(\mathbf{s}). \quad (33)$$

We note that in the framework proposed, the selection of the weighting function space is detached from the trial solutions and the discretization of u . Naturally, and as each w_j furnishes different amounts of information about the solution, an intelligent selection could significantly impact the efficiency of the method, but it is not investigated in this work. Numerical integrations over the problem domain for the evaluation of the associated weighted residuals (Equation (4)) are performed using the trapezoidal rule on a regular 128×128 grid.

Coarse-Grained Implicit Solver: The coarse-grained implicit solver, which lies at the center of the proposed architecture, is obtained by employing a regular, linear, finite element discretization grid of 16×16 triangular pairs for PANIS and 8×8 for mPANIS. Each of the resulting 512 (or 128) triangular elements is assumed to have a constant permeability, which is summarily represented by the vector \mathbf{X} (Equation (14)). The solution of the corresponding discretized equations gives rise to the nodal values which are represented by the vector \mathbf{Y} (Equation (14)).

A summary of the most important dimensions of the models considered is contained in Table 1.

4.1.1 Comparison for Different Volume Fractions

In the following illustrations the predictive accuracy of PANIS will be demonstrated and compared against PINO for various volume fractions VF . Both models were trained for input fields $c(\mathbf{s}; \mathbf{x})$ corresponding to $VF = 50\%$. Subsequently, their predictive performance was tested for $c(\mathbf{s}; \mathbf{x})$ corresponding to a range of different VFs. The convergence of the ELBO during training of PANIS is depicted in Figure 2. Lastly, for all the subsequent illustrations presented in subsections 4.1 and 4.2 the hyperparameters of Algorithm 1 are set $\lambda = 10^4$, $N = 289$ and $M = 100$ ($M = 200$ for subsection 4.2).

⁶Other such functions could be readily employed.

Variable	PANIS	mPANIS	PINO
\mathbf{x}	1024	1024	—
\mathbf{y}	4096	4096	—
\mathbf{X}	289	81	—
\mathbf{Y}	289	81	—
(model parameters) ψ	7956	415112	13140737
ψ_x	5065	12801	—
Wall Clock Time (min)	≈ 10	≈ 807	≈ 2195
Resolution of $c(\mathbf{s}; \mathbf{x})$	128	128	128
Resolution of $u(\mathbf{s})$	128	128	128

Table 1: Most important dimensions of PANIS, mPANIS and PINO.

Volume Fraction (VF)	R^2 (PINO)	R^2 (PANIS)
10 %	-2.749	0.951
20 %	0.510	0.962
30 %	0.911	0.969
40 %	0.967	0.970
50 % (training)	0.985	0.971
60 %	0.988	0.964
70 %	0.983	0.963
80 %	0.968	0.953
90 %	0.911	0.928

Table 2: Predictive accuracy in terms of R^2 (the closer to 1 it is, the better) for PANIS and PINO when tested on various VF values while trained only on $VF = 50\%$.

We note that PINO gives better predictions when it is used in a hybrid mode, i.e. when both data-driven and physics-informed terms are used in the loss function [43]. In the remainder of the paper, we focus purely on physics-informed versions for a fair comparison. Nevertheless, we have conducted one comparison between PANIS and the purely data-based FNO (i.e. the data-based version of PINO) in Figure 4 to demonstrate the competitiveness of PANIS even against well-established data-driven methods such as FNO.

The performance of the two models (PANIS and PINO) is similar for in-distribution predictions, as can be seen in Figure 5. The mean prediction in both cases is close to the ground truth, as seen from the coefficient of determination R^2 . However, PANIS provides uncertainty bounds for the predicted solution, in contrast to PINO, which yields only point estimates for the PDE solution. When both models are inquired in out-of-distribution conditions (i.e. different volume fraction VF), PANIS fully retains its predictive accuracy in contrast to PINO which struggles as seen in Table 2. The latter depicts the R^2 score under various VF s. Due to the physics-aware, implicit solver which lies at the center of its architecture, PANIS is capable of retaining the predictive accuracy for every VF examined, as opposed to PINO, whose accuracy decreases significantly as the volume fraction VF deviates notably from the one used for training, i.e. $VF = 50\%$.

4.1.2 Comparison for Different Dimension of the parametric input \mathbf{x}

In addition, we examined the comparative performance of the aforementioned models for different dimensions $d_{\mathbf{x}}$ of the parametric input \mathbf{x} , which affects the permeability field as explained in Section 4.1. As it can be seen from Table 3, although the predictive accuracy of both models decreases as the parametric input increases, it remains very high even when the parametric input is 1024. We emphasize, however, that the number of training parameters ψ for PANIS is $O(10^4)$ in contrast to PINO, which employs approximately $O(10^7)$ (Table 1). The utilization of the coarse-grained implicit solver enables the reduction of complexity and leads to comparably good results with approximately **three orders of magnitude** fewer parameters.

4.1.3 Comparison for Different Boundary Conditions

In the following illustrations, we focus on a challenging test for the generalization capability of any data-driven scheme. In particular, we report the accuracy of the trained models when called upon to make predictions under different boundary conditions from the ones used to train the models. For this purpose, we train both models with the same conditions as in Equation (30) i.e. $u_0 = 0$, and we test them for 2 very different Dirichlet boundary conditions. The

d_x (dimension of \mathbf{x})	R^2 (PINO)	R^2 (PANIS)
64	0.988	0.982
256	0.987	0.979
1024	0.985	0.971

Table 3: Coefficient of determination R^2 for PINO and PANIS for various parametric inputs \mathbf{x} , when trained on $VF = 50\%$, $u_0 = 0$.

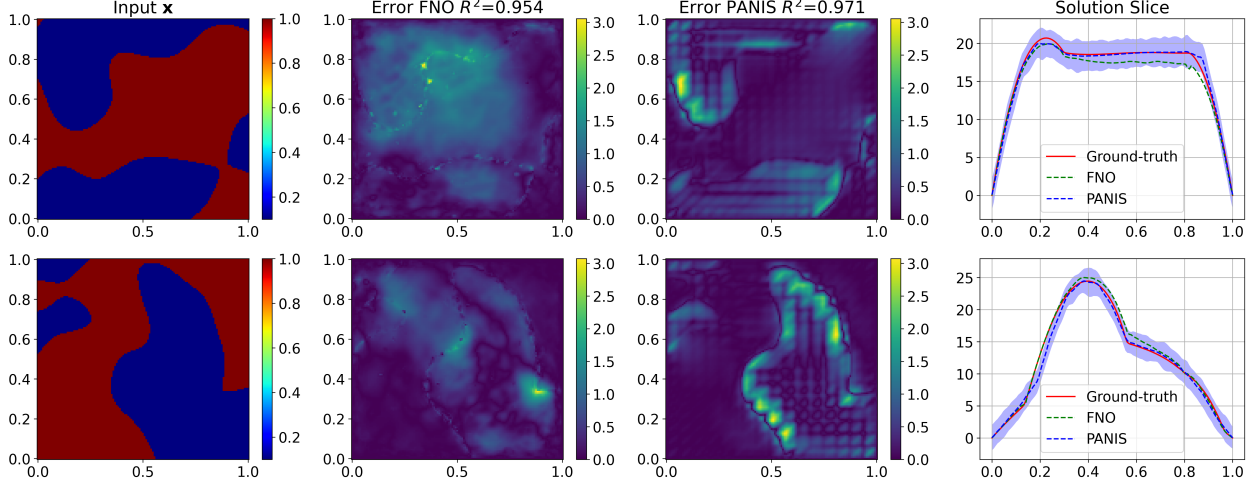


Figure 4: Predictive accuracy of FNO and PANIS when trained and tested on microstructures with $VF = 50\%$. The right column shows a one-dimensional slice of the solution along the vertical line from $(0.5, 0)$ to $(0.5, 1.0)$. The shaded blue area corresponds to ± 2 posterior standard deviations computed as described in Algorithm 2.

first corresponds merely to an offset the BCs i.e. for $u_0 = 10$. The comparison is conducted in terms of relative L_2 error ϵ (Equation (19)) as shown in Table 4. We can observe that PINO fails to predict that the solution simply needs to be shifted by 10 which leads to a high ϵ -value. In contrast, PANIS retains intact its predictive accuracy.

The second boundary condition considered deviates much more from $u_0 = 0$ used for training, and in particular, we employed:

$$u_0(s_1, s_2) = \begin{cases} 10 + 5 \sin\left(\frac{\pi}{2}s_2\right), & \text{if } s_1 = 0, \quad 0 \leq s_2 \leq 1, \\ 10 + 5 \sin\left(\frac{\pi}{2}(s_1 + 1)\right), & \text{if } s_2 = 1, \quad 0 \leq s_1 \leq 1, \\ 10 - 5 \sin\left(\frac{\pi}{2}(s_2 + 1)\right), & \text{if } s_1 = 1, \quad 0 \leq s_2 \leq 1, \\ 10 - 5 \sin\left(\frac{\pi}{2}(s_1)\right), & \text{if } s_2 = 0, \quad 0 \leq s_1 \leq 1. \end{cases} \quad (34)$$

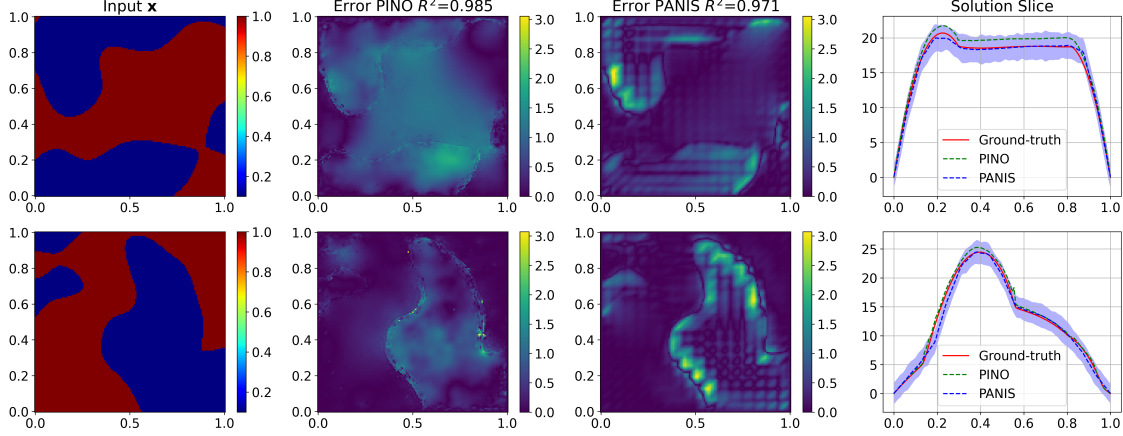
Indicative predictions provided by both models for this non-trivial case are presented in Figure 6. In Table 4, we observe that as in the previous case, and due to the embedded physics, the performance of PANIS is not affected by the change of boundary conditions, whereas the predictions of PINO deteriorate drastically.

Boundary Condition Type	ϵ (PINO)	ϵ (PANIS)
$u_0 = 0$ (training)	0.0381	0.0589
$u_0 = 10$	0.4581	0.0368
u_0 as in Equation 34	0.4763	0.0347

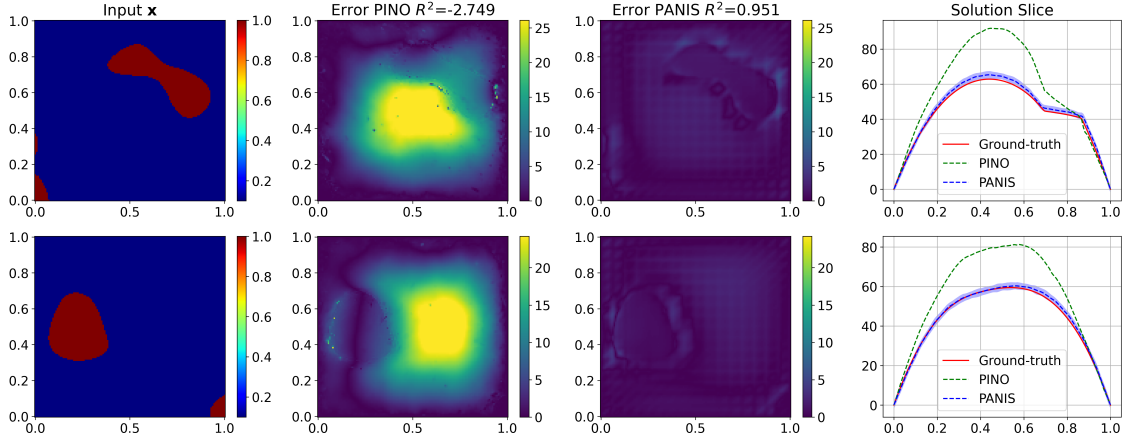
Table 4: Comparison of relative L_2 error ϵ (the smaller, the better) when tested under different boundary conditions.

4.2 Non-Linear Poisson Equation

In this subsection, we assess the performance of the proposed model on a non-linear PDE. We note that no adaptations or changes are needed as the sole conduit of information is the weighted residuals. As a result, the training algorithm



(a) Predictive accuracy of PANIS and PINO when trained and tested on microstructures with $VF = 50 \%$.



(b) **Out of distribution Prediction:** Predictive accuracy of PANIS and PINO when trained on microstructures with $VF = 50 \%$ and tested on $VF = 10 \%$.

Figure 5: Comparison between PANIS and PINO.

merely requires the computation of the residuals and their derivatives with respect to the model parameters (with automatic differentiation).

We consider the same conservation law, which in terms of the flux vector \mathbf{q} , can be written as:

$$\nabla \cdot \mathbf{q} = f, \quad \mathbf{s} \in \Omega = [0, 1] \times [0, 1] \quad (35)$$

which is complemented by a *non-linear* constitutive law of the form:

$$\mathbf{q}(\mathbf{s}) = -c(\mathbf{s}; \mathbf{x}) e^{\alpha(u(\mathbf{s}) - \bar{u})} \nabla u(\mathbf{s}). \quad (36)$$

and Dirichlet boundary condition $u = u_0$, $\mathbf{s} \in \Gamma_D$ as before. The field $c(\mathbf{x}, \mathbf{s})$ is defined as described in subsection 4.1, and α , \bar{u} ⁷ are two additional scalar parameters (assumed to be independent of \mathbf{s}). It is noted that α (and secondarily \bar{u}) controls the degree of non-linearity. For $\alpha = 0$, Equation 35 will take the same form as in Equation 30, and as α increases, so does the nonlinearity in the governing PDE.

The most significant adjustment pertains to the implicit solver that lies at the center of the architecture proposed. Apart from being lower-dimensional and more efficient to solve, one is at liberty to induce as much physical insight and complexity [49]. In this work, we adopt the same discretization explained before and a constitutive law of the same

⁷The values $\alpha = 0.05$ and $\bar{u} = 5$ were used in the subsequent numerical results.

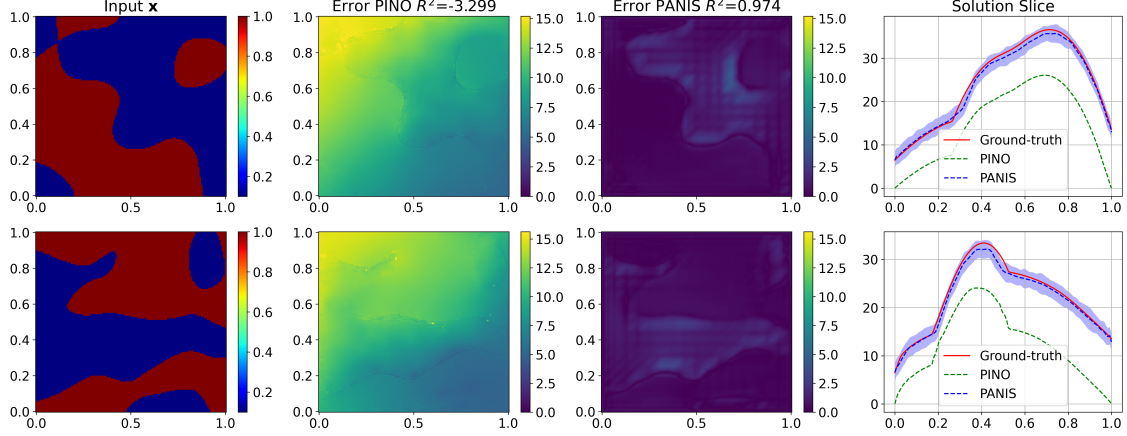


Figure 6: Comparison between PANIS and PINO when trained on $VF = 50\%$, $u_0 = 0$ and tested on $VF = 50\%$, u_0 as described in Equation (34).

Volume Fraction (VF)	Boundary Condition Type	ϵ (PANIS)
10 %	$u_0 = 0$ everywhere	0.0541
20 %	$u_0 = 0$ everywhere	0.0714
30 %	$u_0 = 0$ everywhere	0.0770
40 %	$u_0 = 0$ everywhere	0.0854
50 % (training)	$u_0 = 0$ everywhere	0.0904
60 %	$u_0 = 0$ everywhere	0.0966
70 %	$u_0 = 0$ everywhere	0.1025
80 %	$u_0 = 0$ everywhere	0.1054
90 %	$u_0 = 0$ everywhere	0.1022
50 %	$u_0 = 10$ everywhere	0.0449
50 %	u_0 as in Equation 34	0.0442

Table 5: Relative L_2 error ϵ between PANIS and the ground-truth of the non-linear PDE for various out-of-distribution cases.

nonlinear form as in Equation (36), where in each element of the coarse-grained model instead of $c(s; \mathbf{x})$ we have the learnable parameters denoted by \mathbf{X} (i.e. a and \bar{u} have the same values). We note that one could adopt a different form for the constitutive law or make the corresponding a , \bar{u} learnable as well. In order to solve the corresponding non-linear system of equations, i.e. to determine $\mathbf{Y}(\mathbf{X})$, we employed Newton’s iterative method. This was achieved in a fully vectorized way, such that PyTorch can backpropagate through the computational graph for computation of the gradients needed for estimating the derivatives of the ELBO. In order to further expedite the computations, we initialized the model parameters to the ones found for the linear case, i.e. $a = 0$ (section 4.1) and subsequently increased the a gradually per iteration until the final value of $a = 0.05$ was reached. This provides a natural tempering mechanism that can expedite and stabilize convergence. In addition, and if this is of interest, it enables one to automatically obtain surrogates for intermediate values of the constitutive parameter a which could be used for predictive purposes or sensitivity analysis.

In Figure 7, we show the predictive performance of PANIS for two indicative samples. The predictive accuracy remains high as previously, demonstrating that the proposed framework can also be used effectively in non-linear, parametric PDEs. In out-of-distribution settings as those obtained by altering the volume fraction or the boundary conditions (see sections 4.1.1 and 4.1.3), PANIS retains intact its prediction accuracy as it can be seen in Table 5.

4.3 Multiscale PDE

In this subsection, we demonstrate the multiscale version of the proposed framework (i.e. mPANIS) as described in Section 3. To this end, we consider the PDE of Equation (30) and material property fields obtained for $l = 0.05$ (instead of $l = 0.25$ used in the previous examples). As a result $c(s; \mathbf{x})$ exhibits finer scale fluctuations (see indicative examples shown in Figure 3). For all the subsequent illustrations presented in subsection 4.3 we set $\lambda = 10^{2.2}$, $N = 4096$ and $M = 1500$ (see Algorithm 3), while the number of \mathbf{x} -samples used in training was $K = 100$.

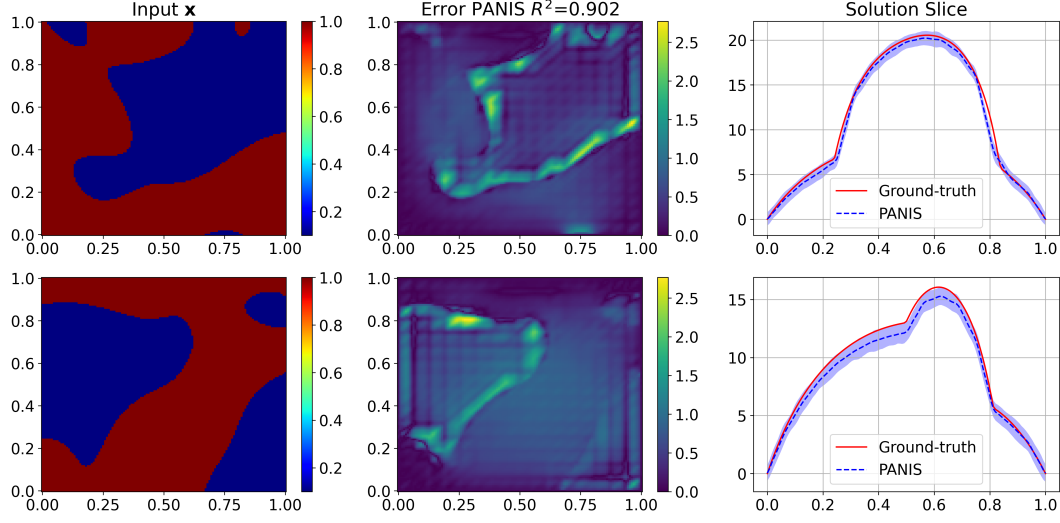


Figure 7: Predictions obtained with PANIS for the non-linear PDE of Equation (35) and microstructures generated with $l = 0.25$, $VF = 50\%$ and $u_0 = 0$.

In Figure 8, we show the results obtained by PANIS and mPANIS for indicative microstructures⁸ as well as the R^2 score over the validation dataset. One readily notes that despite the fact that the true solution is dominated by low-frequency components, PANIS fails to capture them because it ignores the finer-scale fluctuations. As explained in Section 3 these might be small but have a significant effect on the corresponding weighted residuals. In contrast, under mPANIS where such fluctuations are accounted for, one is able to capture the low-frequency components of the solution as well probabilistic predictive estimates.

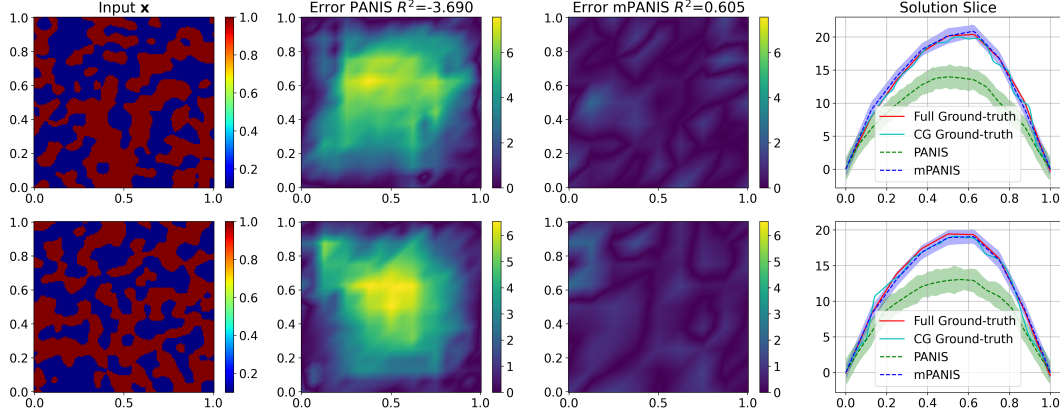


Figure 8: Prediction of PANIS and mPANIS for two indicative inputs ($l = 0.05$, $VF = 50\%$ and $u_0 = 0$).

In Figure 9, we compare the predictive accuracy of mPANIS with PINO. We note that PINO tries to resolve the full-order solution. Despite the fact that mPANIS provides probabilistic solutions and that it employs roughly *two orders of magnitude* fewer parameters and has a training time that is ≈ 3 times lower (wall clock time in the same machine - see Table 3), the two models have similar accuracy when compared to the full-order solution.

With regards to the number of training parameters and as noted in Section 3, this depends on K i.e. the number of x -samples used in training. We had argued therein that the model architecture is such that it saturates with a small K . The validity of this hypothesis is investigated in Figure 10 which depicts the evolution of the two error metrics employed as a function of K . One can see that both stabilize for $K < 100$ beyond which little improvement can be expected.

⁸Similar results are observed for any such input microstructure

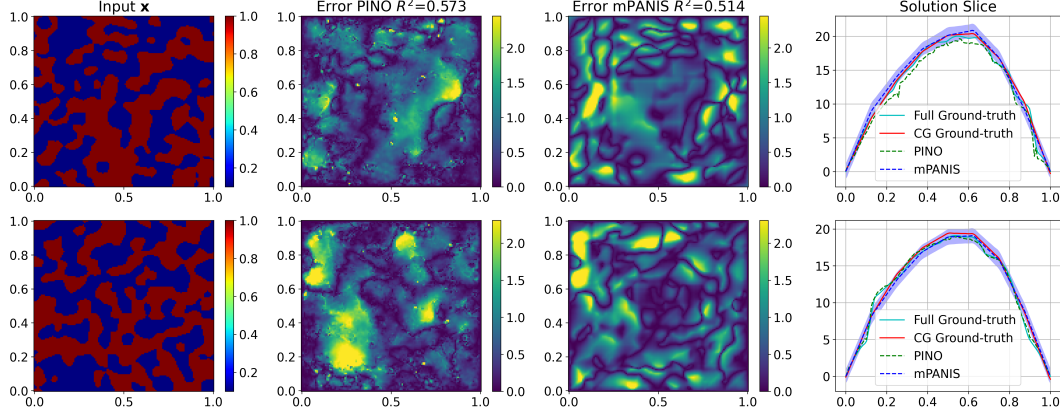


Figure 9: Comparison between PANIS and PINO for conductivity fields with $l = 0.05$, $VF = 50\%$ and $u_0 = 0$ (In-distribution predictions).

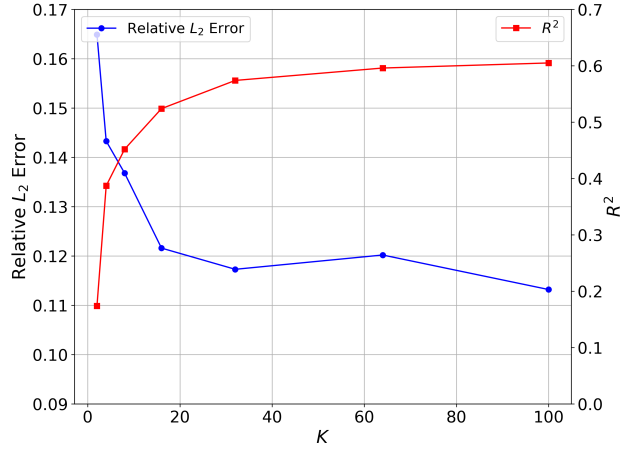


Figure 10: Predictive accuracy of mPANIS in terms of R^2 and relative L_2 error ϵ with respect to the number K of atoms x_k (Equation (24)). We observe that mPANIS saturates with fewer than ~ 50 such atoms.

Volume Fraction (VF)	Boundary Condition Type	ϵ (mPANIS)	ϵ (PINO)
10 %	$u_0 = 0$ everywhere	0.2240	0.5710
20 %	$u_0 = 0$ everywhere	0.1793	0.4593
30 %	$u_0 = 0$ everywhere	0.1339	0.3321
40 %	$u_0 = 0$ everywhere	0.1131	0.2049
50 % (training)	$u_0 = 0$ everywhere	0.1134	0.1029
60 %	$u_0 = 0$ everywhere	0.1112	0.1078
70 %	$u_0 = 0$ everywhere	0.1450	0.1315
80 %	$u_0 = 0$ everywhere	0.2156	0.1920
90 %	$u_0 = 0$ everywhere	0.3438	0.9850
50 %	$u_0 = 10$ everywhere	0.0634	0.5115
50 %	u_0 as in Equation 34	0.0671	0.5225

Table 6: Comparison of relative L_2 error ϵ between PANIS and PINO with the ground-truth for various out-of-distribution cases and $l = 0.05$.

Finally and with regards to out-of-distribution predictions i.e. for different VF s or different BCs, mPANIS generally outperforms PINO and in most cases reported in Table 6 by a quite significant margin despite being much more light-weight as explained above.

5 Conclusions

We have proposed a novel probabilistic, physics-aware framework for constructing surrogates of parametric PDEs. The most notable and novel characteristics of (m)PANIS are:

- it is based on a physics-inspired architecture involving a coarse-grained, implicit solver that introduces a valuable informational bottleneck, which significantly limits the number of trainable parameters and leads to robust generalization.
- it efficiently learns the map between the parametric input and the solution of the PDE by using randomized weighted residuals as informational probes. The trained surrogate provides fully probabilistic predictions that reflect epistemic and model uncertainties,
- it can successfully learn the dominant low-frequency component of the solution in challenging, multiscale PDEs by relying solely on the information from the weighted residuals.
- it yields probabilistic predictions of similar accuracy with PINO and outperforms it in various out-of-distribution cases while being much more lightweight.

The framework introduced provides a multitude of possibilities both in terms of methodological aspects as well as potential applications, the most important of which we enumerate below.

The first pertains to the weighting functions employed. As discussed in section 2.3, weighted residuals are used as probes that extract information from the governing PDE. Naturally, and depending on the problem’s particulars, their informational content can vary drastically but can nevertheless be quantified in the context of the probabilistic framework adopted through the ELBO. One can therefore envision improving drastically the efficiency of the method by using, adaptively, weighting functions/residuals that maximize the informational gain. Another opportunity for *adaptive learning* arises in the context of mPANIS and the empirical approximation of the input density through K atoms \mathbf{x}_k (section 3). As mentioned therein, the number of training parameters that capture the fine-scale fluctuations of the solution i.e. $\{\mathbf{y}'_{f,k}\}_{k=1}^K$ is proportional to K . One could, therefore, envision progressively increasing K by adaptively incorporating new \mathbf{x}_k ’s (and associated $\mathbf{y}'_{f,k}$) on the basis of their ELBO contribution, i.e. the information they furnish. On the methodological front, we finally note the possibility of using a tempering scheme by progressively increasing λ (section 2.2) or alternative forms of the virtual likelihoods which could accelerate convergence.

In terms of applications, an important extension involves dynamical problems. While weighted residuals can be used again to incorporate the PDE in the learning objectives, their dependence on time poses challenges as well as offers several possibilities in terms of enforcement using, e.g. a (linear) multistep method or space-time finite elements [87]. Finally, the most important application pertains to inverse design, i.e. the identification of microstructures \mathbf{x} that achieve target or extremal properties. The inexpensive surrogate developed, particularly in the multiscale setting, can significantly accelerate this search not only because it can yield accurate predictions faster than the PDE-solver [88] but also because, through the use of latent variables (\mathbf{X}, \mathbf{Y} in our case) one can obtain derivatives of the response. Due to the discrete nature of the microstructure \mathbf{x} (and irrespective of the cost of the PDE-solver), these derivatives are not available in the original formulation of the problem.

References

- [1] Salvatore Torquato and Henry W Haslach Jr. Random heterogeneous materials: microstructure and macroscopic properties. *Appl. Mech. Rev.*, 55(4):B62–B63, 2002.
- [2] George Stefanou, Dimitrios Savvas, and Panagiotis Metsis. Random Material Property Fields of 3D Concrete Microstructures Based on CT Image Reconstruction. *Materials*, 14(6):1423, January 2021. Number: 6 Publisher: Multidisciplinary Digital Publishing Institute.
- [3] Yuksel C. Yabansu, Patrick Altschuh, Johannes Hötzer, Michael Selzer, Britta Nestler, and Surya R. Kalidindi. A digital workflow for learning the reduced-order structure-property linkages for permeability of porous membranes. *Acta Materialia*, 195:668–680, August 2020.
- [4] Jitesh H Panchal, Surya R Kalidindi, and David L McDowell. Key computational modeling issues in integrated computational materials engineering. *Computer-Aided Design*, 45(1):4–25, 2013.
- [5] Raymundo Arróyave and David L. McDowell. Systems Approaches to Materials Design: Past, Present, and Future. *Annual Review of Materials Research*, 49(1):103–126, 2019. _eprint: <https://doi.org/10.1146/annurev-matsci-070218-125955>.

- [6] Xian Yeow Lee, Joshua R. Waite, Chih-Hsuan Yang, Balaji Sesha Sarath Pokuri, Ameya Joshi, Aditya Balu, Chinmay Hegde, Baskar Ganapathysubramanian, and Soumik Sarkar. Fast inverse design of microstructures via generative invariance networks. *Nature Computational Science*, 1(3):229–238, March 2021.
- [7] Ankit Agrawal and Alok Choudhary. Perspective: Materials informatics and big data: Realization of the “fourth paradigm” of science in materials science. *APL Materials*, 4(5):053208, May 2016. Publisher: American Institute of Physics.
- [8] Surya R Kalidindi. *Hierarchical materials informatics: novel analytics for materials data*. Elsevier, 2015.
- [9] Stefano Curtarolo, Gus L. W. Hart, Marco Buongiorno Nardelli, Natalio Mingo, Stefano Sanvito, and Ohad Levy. The high-throughput highway to computational materials design. *Nature Materials*, 12(3):191–201, March 2013. Number: 3 Publisher: Nature Publishing Group.
- [10] Zijiang Yang, Yuksel C. Yabansu, Dipendra Jha, Wei-keng Liao, Alok N. Choudhary, Surya R. Kalidindi, and Ankit Agrawal. Establishing structure-property localization linkages for elastic deformation of three-dimensional high contrast composites using deep learning approaches. *Acta Materialia*, 166:335–345, March 2019.
- [11] Lu Lu, Pengzhan Jin, and George Em Karniadakis. Deeponet: Learning nonlinear operators for identifying differential equations based on the universal approximation theorem of operators. *arXiv preprint arXiv:1910.03193*, 2019.
- [12] Zongyi Li, Nikola Kovachki, Kamyar Azizzadenesheli, Burigede Liu, Kaushik Bhattacharya, Andrew Stuart, and Anima Anandkumar. Neural operator: Graph kernel network for partial differential equations. *arXiv preprint arXiv:2003.03485*, 2020.
- [13] Zongyi Li, Nikola Kovachki, Kamyar Azizzadenesheli, Burigede Liu, Kaushik Bhattacharya, Andrew Stuart, and Anima Anandkumar. Fourier neural operator for parametric partial differential equations. *arXiv preprint arXiv:2010.08895*, 2020.
- [14] Huaqian You, Quinn Zhang, Colton J. Ross, Chung-Hao Lee, and Yue Yu. Learning deep Implicit Fourier Neural Operators (IFNOs) with applications to heterogeneous material modeling. *Computer Methods in Applied Mechanics and Engineering*, 398:115296, August 2022.
- [15] George Em Karniadakis, Ioannis G Kevrekidis, Lu Lu, Paris Perdikaris, Sifan Wang, and Liu Yang. Physics-informed machine learning. *Nature Reviews Physics*, 3(6):422–440, 2021.
- [16] P. S. Koutsourelakis, N. Zabaras, and M. Girolami. Special Issue: Big data and predictive computational modeling. *Journal of Computational Physics*, 321:1252–1254, September 2016. Publisher: Elsevier BV.
- [17] Maziar Raissi, Paris Perdikaris, and George Em Karniadakis. Physics informed deep learning (part i): Data-driven solutions of nonlinear partial differential equations. *arXiv preprint arXiv:1711.10561*, 2017.
- [18] Sifan Wang, Hanwen Wang, and Paris Perdikaris. Learning the solution operator of parametric partial differential equations with physics-informed deeponets. *Science advances*, 7(40):eabi8605, 2021.
- [19] Arnaud Vadeboncoeur, Ieva Kazlauskaitė, Yanni Papandreou, Fehmi Cirak, Mark Girolami, and Omer Deniz Akyildiz. Random grid neural processes for parametric partial differential equations. In *International Conference on Machine Learning*, pages 34759–34778. PMLR, 2023.
- [20] Yin hao Zhu, Nicholas Zabaras, Phaedon-Stelios Koutsourelakis, and Paris Perdikaris. Physics-constrained deep learning for high-dimensional surrogate modeling and uncertainty quantification without labeled data. *Journal of Computational Physics*, 394:56–81, 2019.
- [21] Maximilian Rixner and Phaedon-Stelios Koutsourelakis. A probabilistic generative model for semi-supervised training of coarse-grained surrogates and enforcing physical constraints through virtual observables. *Journal of Computational Physics*, 434:110218, 2021.
- [22] Yibo Yang and Paris Perdikaris. Adversarial uncertainty quantification in physics-informed neural networks. *Journal of Computational Physics*, 394:136–152, 2019.
- [23] Sebastian Kaltenbach and Phaedon-Stelios Koutsourelakis. Incorporating physical constraints in a deep probabilistic machine learning framework for coarse-graining dynamical systems. *Journal of Computational Physics*, 419:109673, 2020.
- [24] Maziar Raissi and George Em Karniadakis. Hidden physics models: Machine learning of nonlinear partial differential equations. *Journal of Computational Physics*, 357:125–141, 2018.
- [25] Bing Yu et al. The deep ritz method: a deep learning-based numerical algorithm for solving variational problems. *Communications in Mathematics and Statistics*, 6(1):1–12, 2018.

- [26] Sung Wook Kim, Iljeok Kim, Jonghwan Lee, and Seungchul Lee. Knowledge integration into deep learning in dynamical systems: an overview and taxonomy. *Journal of Mechanical Science and Technology*, 35:1331–1342, 2021.
- [27] Ilias Bilionis and Nicholas Zabaras. Multi-output local gaussian process regression: Applications to uncertainty quantification. *Journal of Computational Physics*, 231(17):5718–5746, 2012.
- [28] Alfio Quarteroni, Andrea Manzoni, and Federico Negri. *Reduced basis methods for partial differential equations: an introduction*, volume 92. Springer, 2015.
- [29] Jan S Hesthaven, Gianluigi Rozza, Benjamin Stamm, et al. *Certified reduced basis methods for parametrized partial differential equations*, volume 590. Springer, 2016.
- [30] Bernard Haasdonk. Reduced basis methods for parametrized pdes—a tutorial introduction for stationary and instationary problems. *Model reduction and approximation: theory and algorithms*, 15:65, 2017.
- [31] Adam P. Generale and Surya R. Kalidindi. Reduced-order models for microstructure-sensitive effective thermal conductivity of woven ceramic matrix composites with residual porosity. *Composite Structures*, 274:114399, October 2021.
- [32] Sepideh Hashemi, Baskar Ganapathysubramanian, Stephen Casey, Ji Su, and Surya R. Kalidindi. Feature engineering for microstructure-property mapping in organic photovoltaics. *arXiv:2111.01897 [cond-mat]*, November 2021. arXiv: 2111.01897.
- [33] Surya R. Kalidindi. Feature engineering of material structure for AI-based materials knowledge systems. *Journal of Applied Physics*, 128(4):041103, July 2020. Publisher: American Institute of Physics.
- [34] Bin Wen and Nicholas Zabaras. A multiscale approach for model reduction of random microstructures. *Computational Materials Science*, 63:269–285, October 2012.
- [35] Ian Goodfellow, Yoshua Bengio, and Aaron Courville. *Deep Learning*. MIT Press, 2016. <http://www.deeplearningbook.org>.
- [36] Jiequn Han, Arnulf Jentzen, and Weinan E. Solving high-dimensional partial differential equations using deep learning. *Proceedings of the National Academy of Sciences*, 115(34):8505–8510, 2018.
- [37] Justin Sirignano and Konstantinos Spiliopoulos. Dgm: A deep learning algorithm for solving partial differential equations. *Journal of computational physics*, 375:1339–1364, 2018.
- [38] Zhen Li and Zuoqiang Shi. Deep residual learning and pdes on manifold. *arXiv preprint arXiv:1708.05115*, 2017.
- [39] Yibo Yang and Paris Perdikaris. Conditional deep surrogate models for stochastic, high-dimensional, and multi-fidelity systems. *Computational Mechanics*, 64:417–434, 2019.
- [40] Yinhao Zhu and Nicholas Zabaras. Bayesian deep convolutional encoder–decoder networks for surrogate modeling and uncertainty quantification. *Journal of Computational Physics*, 366:415–447, 2018.
- [41] Shaoxing Mo, Yinhao Zhu, Nicholas Zabaras, Xiaqing Shi, and Jichun Wu. Deep convolutional encoder-decoder networks for uncertainty quantification of dynamic multiphase flow in heterogeneous media. *Water Resources Research*, 55(1):703–728, 2019.
- [42] Nikola Kovachki, Zongyi Li, Burigede Liu, Kamyar Azizzadenesheli, Kaushik Bhattacharya, Andrew Stuart, and Anima Anandkumar. Neural operator: Learning maps between function spaces. *arXiv preprint arXiv:2108.08481*, 2021.
- [43] Zongyi Li, Hongkai Zheng, Nikola Kovachki, David Jin, Haoxuan Chen, Burigede Liu, Kamyar Azizzadenesheli, and Anima Anandkumar. Physics-informed neural operator for learning partial differential equations. *arXiv preprint arXiv:2111.03794*, 2021.
- [44] Tapas Tripura and Souvik Chakraborty. Wavelet neural operator: a neural operator for parametric partial differential equations. *arXiv preprint arXiv:2205.02191*, 2022.
- [45] Bogdan Raonic, Roberto Molinaro, Tim De Ryck, Tobias Rohner, Francesca Bartolucci, Rima Alaifari, Siddhartha Mishra, and Emmanuel de Bézenac. Convolutional neural operators for robust and accurate learning of pdes. *Advances in Neural Information Processing Systems*, 36, 2024.
- [46] V. S. Fanaskov and I. V. Oseledets. Spectral Neural Operators. *Doklady Mathematics*, 108(2):S226–S232, December 2023.
- [47] Miles Cranmer, Alvaro Sanchez-Gonzalez, Peter Battaglia, Rui Xu, Kyle Cranmer, David Spergel, and Shirley Ho. Discovering Symbolic Models from Deep Learning with Inductive Biases. *arXiv:2006.11287 [astro-ph, physics:physics, stat]*, June 2020.

- [48] Jonas Köhler, Leon Klein, and Frank Noé. Equivariant flows: exact likelihood generative learning for symmetric densities. In *International conference on machine learning*, pages 5361–5370. PMLR, 2020.
- [49] Constantin Grigo and Phaeton-Stelios Koutsourelakis. A physics-aware, probabilistic machine learning framework for coarse-graining high-dimensional systems in the Small Data regime. *Journal of Computational Physics*, 397:108842, November 2019.
- [50] Shailesh Garg and Souvik Chakraborty. Variational bayes deep operator network: A data-driven bayesian solver for parametric differential equations. *arXiv preprint arXiv:2206.05655*, 2022.
- [51] Arnaud Vadeboncoeur, Ömer Deniz Akyildiz, Ieva Kazlauskaitė, Mark Girolami, and Fehmi Cirak. Fully probabilistic deep models for forward and inverse problems in parametric pdes. *Journal of Computational Physics*, 491:112369, 2023.
- [52] B. Van Bavel, Y. Zhao, M. G. R. Faes, D. Vandepitte, and D. Moens. Efficient quantification of composite spatial variability: A multiscale framework that captures intercorrelation. *Composite Structures*, 323:117462, November 2023.
- [53] BA Finlayson, editor. *The method of weighted residuals and variational principles, with application in fluid mechanics, heat and mass transfer, Volume 87*. Academic Press, New York, February 1972.
- [54] Ehsan Kharazmi, Zhongqiang Zhang, and George E. M. Karniadakis. hp-VPINNs: Variational physics-informed neural networks with domain decomposition. *Computer Methods in Applied Mechanics and Engineering*, 374:113547, February 2021.
- [55] John Paisley, David Blei, and Michael Jordan. Variational bayesian inference with stochastic search. *arXiv preprint arXiv:1206.6430*, 2012.
- [56] David M Blei, Alp Kucukelbir, and Jon D McAuliffe. Variational inference: A review for statisticians. *Journal of the American statistical Association*, 112(518):859–877, 2017.
- [57] Tim De Ryck, Ameya D Jagtap, and Siddhartha Mishra. Error estimates for physics-informed neural networks approximating the navier–stokes equations. *IMA Journal of Numerical Analysis*, 44(1):83–119, 2024.
- [58] Aditi Krishnapriyan, Amir Gholami, Shandian Zhe, Robert Kirby, and Michael W Mahoney. Characterizing possible failure modes in physics-informed neural networks. *Advances in Neural Information Processing Systems*, 34:26548–26560, 2021.
- [59] Maziar Raissi, Paris Perdikaris, and George E Karniadakis. Physics-informed neural networks: A deep learning framework for solving forward and inverse problems involving nonlinear partial differential equations. *Journal of Computational physics*, 378:686–707, 2019.
- [60] Mohammad Amin Nabian and Hadi Meidani. A deep neural network surrogate for high-dimensional random partial differential equations. *arXiv preprint arXiv:1806.02957*, 2018.
- [61] William J Morokoff and Russel E Caflisch. Quasi-monte carlo integration. *Journal of computational physics*, 122(2):218–230, 1995.
- [62] Yaohua Zang, Gang Bao, Xiaojing Ye, and Haomin Zhou. Weak adversarial networks for high-dimensional partial differential equations. *Journal of Computational Physics*, 411:109409, 2020.
- [63] Filipe De Avila Bkotlerelbute-Peres, Thomas Economon, and Zico Kolter. Combining differentiable pde solvers and graph neural networks for fluid flow prediction. In *ICML*, pages 2402–2411, 2020.
- [64] Kiwon Um, Robert Brand, Yun Raymond Fei, Philipp Holl, and Nils Thuerey. Solver-in-the-loop: Learning from differentiable physics to interact with iterative pde-solvers. *Advances in Neural Information Processing Systems*, 33:6111–6122, 2020.
- [65] Michael Bartholomew-Biggs, Steven Brown, Bruce Christianson, and Laurence Dixon. Automatic differentiation of algorithms. *Journal of Computational and Applied Mathematics*, 124(1-2):171–190, 2000.
- [66] Atilim Gunes Baydin, Barak A Pearlmutter, Alexey Andreyevich Radul, and Jeffrey Mark Siskind. Automatic differentiation in machine learning: a survey. *Journal of machine learning research*, 18(153):1–43, 2018.
- [67] Antony Jameson. Aerodynamic shape optimization using the adjoint method. *Lectures at the Von Karman Institute, Brussels*, 2003.
- [68] Evangelos M Papoutsis-Kiachagias and Kyriakos C Giannakoglou. Continuous adjoint methods for turbulent flows, applied to shape and topology optimization: industrial applications. *Archives of Computational Methods in Engineering*, 23(2):255–299, 2016.
- [69] Matthew D Hoffman, David M Blei, Chong Wang, and John Paisley. Stochastic variational inference. *Journal of Machine Learning Research*, 2013.

- [70] Diederik P Kingma and Jimmy Ba. Adam: A method for stochastic optimization. *arXiv preprint arXiv:1412.6980*, 2014.
- [71] Yingjie Tian, Yuqi Zhang, and Haibin Zhang. Recent advances in stochastic gradient descent in deep learning. *Mathematics*, 11(3):682, 2023.
- [72] Tommi Vatanen, Tapani Raiko, Harri Valpola, and Yann LeCun. Pushing stochastic gradient towards second-order methods—backpropagation learning with transformations in nonlinearities. In *Neural Information Processing: 20th International Conference, ICONIP 2013, Daegu, Korea, November 3-7, 2013. Proceedings, Part I 20*, pages 442–449. Springer, 2013.
- [73] Durk P Kingma, Tim Salimans, and Max Welling. Variational dropout and the local reparameterization trick. *Advances in neural information processing systems*, 28, 2015.
- [74] Dabao Zhang. A coefficient of determination for generalized linear models. *The American Statistician*, 71(4):310–316, 2017.
- [75] Lu Lu, Xuhui Meng, Shengze Cai, Zhiping Mao, Somdatta Goswami, Zhongqiang Zhang, and George Em Karniadakis. A comprehensive and fair comparison of two neural operators (with practical extensions) based on fair data. *Computer Methods in Applied Mechanics and Engineering*, 393:114778, 2022.
- [76] E Weinan. *Principles of multiscale modeling*. Cambridge University Press, 2011.
- [77] Grigoris Pavliotis and Andrew Stuart. *Multiscale methods: averaging and homogenization*. Springer Science & Business Media, 2008.
- [78] Enrique Sanchez-Palencia and André Zaoui. Homogenization techniques for composite media. *Homogenization techniques for composite media*, 272, 1987.
- [79] Marc GD Geers, Varvara G Kouznetsova, Karel Matouš, and Julien Yvonnet. Homogenization methods and multiscale modeling: nonlinear problems. *Encyclopedia of computational mechanics second edition*, pages 1–34, 2017.
- [80] Zhen Zhang, Yeonjong Shin, and George Em Karniadakis. GFINNs: GENERIC Formalism Informed Neural Networks for Deterministic and Stochastic Dynamical Systems. *arXiv:2109.00092 [cs, math]*, August 2021. arXiv: 2109.00092.
- [81] Quercus Hernandez, Alberto Badias, Francisco Chinesta, and Elias Cueto. Thermodynamics-informed graph neural networks. *arXiv preprint arXiv:2203.01874*, 2022.
- [82] Filippo Masi and Ioannis Stefanou. Multiscale modeling of inelastic materials with thermodynamics-based artificial neural networks (tann). *Computer Methods in Applied Mechanics and Engineering*, 398:115190, 2022.
- [83] Elias Cueto and Francisco Chinesta. Thermodynamics of learning physical phenomena. *Archives of Computational Methods in Engineering*, 30(8):4653–4666, 2023.
- [84] Adam Paszke, Sam Gross, Francisco Massa, Adam Lerer, James Bradbury, Gregory Chanan, Trevor Killeen, Zeming Lin, Natalia Gimelshein, Luca Antiga, et al. Pytorch: An imperative style, high-performance deep learning library. *Advances in neural information processing systems*, 32, 2019.
- [85] Martin S. Alnaes, Jan Blechta, Johan Hake, August Johansson, Benjamin Kehlet, Anders Logg, Chris N. Richardson, Johannes Ring, Marie E. Rognes, and Garth N. Wells. The FEniCS project version 1.5. *Archive of Numerical Software*, 3, 2015.
- [86] Kaushik Bhattacharya, Bamdad Hosseini, Nikola B Kovachki, and Andrew M Stuart. Model reduction and neural networks for parametric pdes. *The SMAI journal of computational mathematics*, 7:121–157, 2021.
- [87] Serge Dumont, Franck Jourdan, and Tarik Madani. 4D Remeshing Using a Space-Time Finite Element Method for Elastodynamics Problems. *Mathematical and Computational Applications*, 23(2):29, June 2018. Number: 2 Publisher: Multidisciplinary Digital Publishing Institute.
- [88] Maximilian Rixner and Phaeton-Stelios Koutsourelakis. Self-supervised optimization of random material microstructures in the small-data regime. *npj Computational Materials*, 8(1):1–11, March 2022. Number: 1 Publisher: Nature Publishing Group.
- [89] Xavier Glorot and Yoshua Bengio. Understanding the difficulty of training deep feedforward neural networks. In *Proceedings of the thirteenth international conference on artificial intelligence and statistics*, pages 249–256. JMLR Workshop and Conference Proceedings, 2010.

A Shallow CNN employed for $X_{\psi_x}(x)$.

The details for the CNN used in the case of PANIS are shown in Table 7 and in Table 8 for mPANIS. The only kind of activation function used is the Softplus activation function. These are used after each convolution/deconvolution layer and before the batch normalization layers, except from the last deconvolution layer. The weights of the convolution/deconvolution layers are initialized by using a Xavier uniform distribution [89].

Layers	Feature Maps	Height \times Width	Number of Parameters
Input	—	129×129	—
Convolution Layer (k3s2p1)	8	65×65	80
Batch Normalization	—	65×65	16
Average Pooling Layer (k2s2)	—	32×32	—
Convolution Layer (k3s1p1)	24	32×32	1752
Batch Normalization	—	32×32	48
Average Pooling Layer (k2s2)	—	16×16	—
Deconvolution Layer (k4s1p1)	8	17×17	3080
Batch Normalization	—	17×17	16
Deconvolution Layer (k3s1p1)	—	17×17	73
In total	40	—	5065

Table 7: Layers of the CNN used in PANIS.

Layers	Feature Maps	Height \times Width	Number of Parameters
Input	—	129×129	—
Convolution Layer (k3s1p1)	8	129×129	80
Batch Normalization	—	129×129	16
Average Pooling Layer (k4s4)	—	32×32	—
Convolution Layer (k3s1p1)	16	32×32	1168
Batch Normalization	—	32×32	32
Average Pooling Layer (k2s2)	—	16×16	—
Convolution Layer (k3s1p1)	32	16×16	4640
Batch Normalization	—	16×16	64
Average Pooling Layer (k2s2)	—	8×8	—
Deconvolution Layer (k3s1p1)	16	8×8	4624
Batch Normalization	—	8×8	32
Deconvolution Layer (k4s1p1)	8	9×9	2056
Batch Normalization	—	9×9	16
Deconvolution Layer (k3s1p1)	—	9×9	73
In total	80	—	12801

Table 8: Layers of the CNN used in mPANIS.

B Coarse-to-Fine Output Map $y(Y)$

In the coarse-grained (CG) model, the solution field in space, i.e. $y_{CG}(s)$, is represented as:

$$u_{CG}(s) = \sum_{J=1}^N Y_J H_J(s), \quad (37)$$

where $N = \dim(Y)$ and H_J are the corresponding shape/basis functions. If e.g. s_J are the nodal points and H_J the usual FE shape functions then $u_{CG}(s_J) = Y_J$.

In the reference, fine-grained (FG) model, the solution field, i.e. $u(s)$, is represented as in Equation (2):

$$u(s) = \sum_{j=1}^n y_j \eta_j(s), \quad (38)$$

where $n = \dim(\mathbf{y})$ and η_j are the corresponding shape/basis functions.

The mapping between \mathbf{Y} and \mathbf{y} is selected so that:

$$u_{CG}(\mathbf{s}) \approx u(\mathbf{s}). \quad (39)$$

One way to quantify the difference/error is e.g.:

$$E = \frac{1}{2} \int_{\Omega} (u_{CG}(\mathbf{s}) - u(\mathbf{s}))^2 d\mathbf{s}. \quad (40)$$

One can readily find that the minimizing E is equivalent to:

$$\mathbf{y} = \mathbf{a}^{-1} \mathbf{B} \mathbf{Y}, \quad (41)$$

where:

- \mathbf{a} is an $n \times n$ matrix with entries $a_{jk} = \int_{\Omega} \eta_j(\mathbf{s}) \eta_k(\mathbf{s}) d\mathbf{s}$
- \mathbf{B} is an $n \times N$ matrix with entries $B_{kJ} = \int_{\Omega} \eta_k(\mathbf{s}) H_J(\mathbf{s}) d\mathbf{s}$.

The matrix $\mathbf{A} = \mathbf{a}^{-1} \mathbf{B}$ in Equation (14) fully defines the coarse-to-fine map and can be pre-computed. As a result, there are no parameters to fine-tune which forces \mathbf{X} (on which \mathbf{Y} depends) to attain the physical meaning discussed in section 2.4.

C ELBO Terms

The computation of the gradient of $\mathcal{F}(\psi)$ with respect to ψ is based on the auto-differentiation capabilities of PyTorch [84, 65]. After each term of the ELBO has been computed, PyTorch automatically back-propagates through the respective graph to obtain the gradient with respect to the training parameters.

Regarding the ELBO used for training PANIS, by substituting Equation (11) in Equation (10), we obtain the following simplified version of the latter:

$$\begin{aligned} \mathcal{F}(\psi) \approx & -\lambda \frac{N}{M} \sum_{m=1}^M \langle |r_{w_{j_m}}(\mathbf{y}, \mathbf{x})| \rangle_{q_{\psi}(\mathbf{x}, \mathbf{y})} \\ & + \langle \log p(\mathbf{y}|\mathbf{x}) \rangle_{q_{\psi}(\mathbf{x}, \mathbf{y})} - \langle \log q_{\psi}(\mathbf{y}|\mathbf{x}) \rangle_{q_{\psi}(\mathbf{x}, \mathbf{y})}, \text{ where } j_m \sim \text{Cat}(N, \frac{1}{N}). \end{aligned} \quad (42)$$

Given that we have access to R samples $\{\mathbf{x}_r\}_{r=1}^R$ and $\{\mathbf{y}_r\}_{r=1}^R$ from the approximate posterior described in Algorithm 1, we approximate the first two terms by Monte Carlo. The second one involves the uninformative multivariate Gaussian prior $\mathcal{N}(\mathbf{y}|\mathbf{0}, \sigma^2 \mathbf{I})$, where $\sigma^2 = 10^{16}$ (see subsections 2.3 and 3.2). The last term is the entropy of $q_{\psi}(\mathbf{y}|\mathbf{x})$ which is calculated closed form exists since $q_{\psi}(\mathbf{y}|\mathbf{x})$ is a multivariate Gaussian distribution. Thus, Equation 42 can be written (up to a constant) as:

$$\begin{aligned} \mathcal{F}(\psi) \approx & -\lambda \frac{N}{MR} \sum_{m=1}^M \sum_{r=1}^R |r_{w_{j_m}}(\mathbf{y}_r, \mathbf{x}_r)| \\ & - \frac{1}{2R\sigma^2} \sum_{r=1}^R \mathbf{y}_r^T \mathbf{y}_r + \frac{1}{2} \log \det(\Sigma_{\psi}), \text{ where } j_m \sim \text{Cat}(N, \frac{1}{N}). \end{aligned} \quad (43)$$

In the case of mPANIS described in subsection 3.2, the same procedure was followed as above starting from Equations 27 and 28 by taking into account that:

- The priors $p(\mathbf{y}_c|\mathbf{x})$ and $p(\mathbf{y}'_f|\mathbf{x})$ have the same form as the prior $p(\mathbf{y}|\mathbf{x})$ in the case of PANIS previously mentioned.
- The entropy term resulting from the degenerate density $\delta(\mathbf{y}'_f - \mathbf{y}'_{f,k})$ (see Equation (25)) will have a zero contribution on the ELBO.

By subsampling a subset $\{\mathbf{x}_r\}_{r=1}^R \subset \{\mathbf{x}_k\}_{k=1}^K$ and the respective subsets $\{\mathbf{y}_{c,r}\}_{r=1}^R$, $\{\mathbf{y}'_{f,r}\}_{r=1}^R$ the equation with which estimations of the ELBO (up to a constant) are made in the case of mPANIS is:

$$\begin{aligned} \mathcal{F}(\psi) \approx & -\lambda \frac{N}{MR} \sum_{m=1}^M \sum_{i=1}^R |r_{w_{j_m}}(\mathbf{y}_{c,r}, \mathbf{y}'_{f,r}, \mathbf{x}_r)| \\ & - \frac{1}{2R\sigma^2} \sum_{i=1}^R (\mathbf{y}_{c,r}^T \mathbf{y}_{c,r} + \mathbf{y}'_{f,r}^T \mathbf{y}'_{f,r}) + \frac{1}{2} \log \det(\Sigma_{\psi}), \text{ where } j_m \sim \text{Cat}(N, \frac{1}{N}). \end{aligned} \quad (44)$$

As one can observe from Equations 43 and 44, when σ is big (as in the cases employed), the second term of the ELBO is approximately equal to zero, and thus it could be completely ignored.